Computational Materials Science 63 (2012) 91–104

Contents lists available at SciVerse ScienceDirect

Computational Materials Science

journal homepage: www.elsevier.com/locate/commatsci

Comparison of spherical and cubical statistical volume elements with respect to convergence, anisotropy, and localization behavior

R. Glüge *, M. Weber, A. Bertram

Universität Magdeburg, Universitätsplatz 2, D-39106, Germany

ARTICLE INFO

Article history:
Received 29 February 2012
Received in revised form 8 May 2012
Accepted 26 May 2012
Available online 29 June 2012

Keywords:
Representative volume element
Statistical volume element
Shape
Anisotropy
Convergence
Localization

ABSTRACT

The statistical volume element (SVE) technique is commonly used for the estimation of the effective properties of a micro-structured material. Mostly, cubical SVEs with periodic boundary conditions are employed, which result in a better convergence, compared to the uniform boundary conditions. In this work, the possibility of using spherical SVEs is discussed, since their use promises a reduction of the influence of the boundary, and thus a more efficient estimation of the effective material properties. We discuss the applicability of boundary conditions which are similar to the periodic boundary conditions to spherical SVEs. Then we assess the convergence (subject 1) of spherical and cubical SVEs to the effective material behavior for the uniform and periodic boundary conditions, focusing on the elastic and plastic properties of a macroscopically isotropic matrix-inclusion material. It is shown that the spherical SVEs perform indeed better than the cubical SVEs. Also, unlike the spherical SVEs, the cubical SVEs with periodic boundary conditions induce a spurious anisotropy (subject 2), which is quantified for the effective elastic properties. Finally, we examine the effect of the periodicity frame on the localization behavior (subject 3) of cubical SVE, since cubical SVE with periodic boundary conditions are commonly used to estimate macroscale material failure. It is demonstrated that the orientation of the periodicity frame affects the overall SVE response significantly. The latter is not observed for spherical SVE.

1. Introduction

The microscale structure of a material can have a considerable effect on the material properties as perceived on the macroscale. Common examples are polycrystals, which may exhibit a crystallographic (crystal orientation) and morphological (grain shape) texture, fiber or particle reinforced composites, foams and laminates. The process of calculating the effective material properties from the arrangement and the properties of the constituents on a smaller scale is termed as homogenization.

For specific material properties, efficient homogenization methods are at hand, see for example Klusemann and Svendsen [26] for the elastic properties, or Fritzen et al. [13] for the yield limit of porous materials. However, in many cases the analytical homogenization is limited, e.g. for the prediction of the crystallographic texture evolution [5]. Then, one follows commonly the pragmatic approach of the RVE or SVE method, which consists of considering a representative section of the material, define appropriate boundary conditions, and solve the initial- and boundary-value problem, usually with the help of numerical methods such as the finite element method. Then, one is able to extract the volume average of the variable of interest, or examine the effect of different microstructures on the overall material behavior. For an account on numerical homogenization by the SVE/RVE method see, e.g., Zohdi and Wriggers [49]. In this work, we will not distinguish strictly between RVE and SVE, which capture the microstructure identically (RVE) or in an approximate sense (SVE). Here, the two terms are used like synonyms.

When focusing on macroscale stress–strain relations, in contrast to analytical techniques, one does not arrive at a closed-form, but obtains an approximation for a specific deformation path. For a coupling with a large-scale FE application, one may use the FE^2 method [44,9,30,38]. However, this is computationally very expensive, and one is interested in a reduction of the numerical costs. A relatively new approach to this problem is the coupling of the RVE-method with the nonuniform transformation field analysis (NTFA [29,12]). Roughly speaking, the RVE method is used to build a database for different deformation modes, from which the actual stress–strain-relations needed in the macroscale calculation are estimated. However, the NTFA is restricted to the small strain setting.

A more direct reduction of the numerical costs of the FE^2 method is the optimization of the RVE, and to apply it simultaneously to a large-scale constitutive law. Then, the RVE calculations are carried out only when and where it is necessary, e.g., when the

* Corresponding author. Tel.: +49 391 67 12592; fax: +49 391 67 12863.
E-mail address: gluege@ovgu.de (R. Glüge).

0927-0256/$ - see front matter © 2012 Elsevier B.V. All rights reserved.
http://dx.doi.org/10.1016/j.commatsci.2012.05.063

straining is large. Also, the RVE itself should be as representative as possible, but still require an acceptable numerical effort. The problem of determining a RVE with a good balance between representativity and numerical expense, arises. It depends on the material under consideration, and has been subject of many studies, e.g., Kanit et al. [23], Xu and Chen [47], Pelissou et al. [39], Salahouelhadj and Haddadi [41]. Another possibility to increase the ratio representativity/numerical effort is to optimize the material section under consideration [42].

Here, we examine the influence of the shape of the RVE. Usually, cubical RVEs are used. We demonstrate that the use of spherical RVEs is advantageous for two reasons. Firstly, the bias due to specific boundary conditions is weaker, since the surface-to-volume ratio is smaller than for cubical RVEs. Secondly, spherical RVEs do not induce a material-independent anisotropy, unlike cubical RVEs with periodic boundary conditions. The reduction of the shape-induced anisotropy has been discussed by Grasset-Bourdel et al. [16], who considered RVEs with shapes that allow for a complete filling of the space. It was found that a hexagonal arrangement is advantageous, compared to a cubic shape. However, the restriction to shapes that allow for a complete filling of the space appears to be unnecessary, since spherical RVE are used routinely for analytical methods [17,43,8], while in numerical calculations the cubical RVEs predominate. Only few exceptions can be found, e.g., Kim et al. [25] and the authors referred to in this work used non-periodic RVEs.

The outline of this work is as follows: We firstly reproduce the fundamentals of the RVE method (Section 2), followed by a discussion of the possible boundary conditions (Section 3) that may be applied to spherical and cubical RVEs (Section 4). In Section 5 the setup for the numerical experiments is described. In Section 6 we examine the convergence while increasing the RVE size for the elastic and plastic properties of a matrix–inclusion-material, and compare different shapes and boundary conditions. In Section 7 we assess the shape-induced anisotropy of the spherical and cubical RVE with periodic boundary conditions by applying them to an effectively isotropic material. Finally we focus on the peculiarities of the localization behavior of the spherical and cubical RVE (Section 8).

1.1. Notation

Throughout the work a direct tensor notation is preferred. If an expression cannot be represented in the direct notation without introducing new conventions, its components are given with respect to orthonormal base vectors $\boldsymbol{e}_i$, using the summation convention. Vectors are symbolized by lowercase bold letters $\boldsymbol{v} = v_i\boldsymbol{e}_i$, second-order tensors by uppercase bold letters $\boldsymbol{T} = T_{ij}\boldsymbol{e}_i \otimes \boldsymbol{e}_j$ or bold Greek letters. The second-order identity tensor is denoted by $\boldsymbol{I}$. Fourth-order tensors are symbolized like $\mathbb{C}$. The dyadic product is defined as $(\boldsymbol{a} \otimes \boldsymbol{b}) \cdot \boldsymbol{c} = (\boldsymbol{b} \cdot \boldsymbol{c})\boldsymbol{a}$. A dot represents a scalar contraction. If more than one scalar contraction is carried out, the number of dots corresponds to the number of contractions, thus $(\boldsymbol{a} \otimes \boldsymbol{b} \otimes \boldsymbol{c}) \cdot\cdot (\boldsymbol{d} \otimes \boldsymbol{e}) = (\boldsymbol{b} \cdot \boldsymbol{d})(\boldsymbol{c} \cdot \boldsymbol{e})\boldsymbol{a}$, $\alpha = \boldsymbol{A} \cdot\cdot \boldsymbol{B}$ and $\boldsymbol{\sigma} = \mathbb{C} \cdot\cdot \boldsymbol{\varepsilon}$. If only one scalar contraction is carried out, the scalar dot is frequently omitted, e.g., $\boldsymbol{v} = \boldsymbol{F}\boldsymbol{w}$, $\boldsymbol{A} = \boldsymbol{B}\boldsymbol{C}$. $\|\boldsymbol{x}\|$ denotes the Frobenius norm.

The position vector of a material point is denoted by $\boldsymbol{x}(\boldsymbol{x}_0, t)$, where $\boldsymbol{x}_0$ indicates the position vector of the same material point in the reference placement. At $t = 0$, $\boldsymbol{x} = \boldsymbol{x}_0$ holds. The partial derivative of a function with respect to t with $\boldsymbol{x}_0$ kept constant is the material time derivative, indicated by a superimposed dot. The index "0" indicates that a function or derivative is to be evaluated in the reference placement or with respect to $\boldsymbol{x}_0$. Ω denotes the domain of the RVE under consideration. All unweighted volume averages over this domain are evaluated in the reference placement, denoted as $\langle\cdot\rangle := \frac{1}{V_0}\int_{\Omega_0} \cdot \, \mathrm{d}V$. A superimposed bar indicates a macroscale-quantity.

1.2. List of symbols

C_{ijkl}	components of the stiffness tetrad with respect to an orthonormal basis
J	$\det\boldsymbol{F}$
ρ	mass density
Ω	domain of the RVE
∇	nabla operator
$\boldsymbol{b}$	mass-specific force density
$\boldsymbol{n}$	surface normal vector
$\boldsymbol{t}$	traction vector $\boldsymbol{t} = \boldsymbol{\sigma} \cdot \boldsymbol{n}$
$\boldsymbol{u}$	displacement vector, $\boldsymbol{u} = \boldsymbol{x} - \boldsymbol{x}_0$
$\boldsymbol{x}$	position vector
$\boldsymbol{\sigma}$	Cauchy stress tensor
$\boldsymbol{\varepsilon}$	linear strain tensor, $\boldsymbol{\varepsilon} = \frac{1}{2}(\boldsymbol{H} + \boldsymbol{H}^T)$
$\boldsymbol{\tau}$	Kirchhoff stress tensor, $\boldsymbol{\tau} = J\boldsymbol{\sigma}$
$\boldsymbol{D}$	rate of deformation tensor, symmetric part of $\boldsymbol{L}$, $\boldsymbol{D} = \frac{1}{2}(\boldsymbol{L} + \boldsymbol{L}^T)$
$\boldsymbol{F}$	deformation gradient, $\boldsymbol{F} = \boldsymbol{x} \otimes \nabla_0$
$\boldsymbol{H}$	displacement gradient, $\boldsymbol{H} = \boldsymbol{F} - \boldsymbol{I} = \boldsymbol{u} \otimes \nabla_0$
$\boldsymbol{L}$	velocity gradient, $\boldsymbol{L} = \dot{\boldsymbol{x}} \otimes \nabla = \dot{\boldsymbol{F}}\boldsymbol{F}^{-1}$
$\boldsymbol{T}$	first Piola–Kirchhoff stress tensor, $\boldsymbol{T} = \det(\boldsymbol{F})\boldsymbol{\sigma}\boldsymbol{F}^{-T}$
$\mathbb{I}$	fourth order identity on symmetric second order tensors
$\mathbb{P}_1$	first isotropic projector, $\mathbb{P}_1 = \frac{1}{3}\boldsymbol{I} \otimes \boldsymbol{I}$
$\mathbb{P}_2$	second isotropic projector, $\mathbb{P}_2 = \mathbb{I} - \mathbb{P}_1$
$\mathbb{P}_{c2}$	second cubic projector
$\mathbb{P}_{c3}$	third cubic projector
HTBC	homogeneous traction boundary conditions
LDBC	linear displacement boundary conditions
PBC	periodic boundary conditions

2. Basic considerations

2.1. Scale separation

The scale separation requires that $l_{\text{micro}} \ll l_{\text{mini}} \ll l_{\text{macro}}$ [18], where l_{micro} refers to the characteristic size of the heterogeneities, l_{mini} to the RVE size and l_{macro} to the dimensions of the body. $l_{\text{micro}} \ll l_{\text{mini}}$ ensures the representativity of the RVE, while $l_{\text{mini}} \ll l_{\text{macro}}$ is necessary if one wants to consider the RVE as a material point on the macroscale.

2.2. Equilibrium equations

The local balances of linear and angular momentum require

$$\boldsymbol{\sigma} \cdot \nabla = \rho(\ddot{\boldsymbol{x}} - \boldsymbol{b}), \qquad \boldsymbol{\sigma} = \boldsymbol{\sigma}^T, \tag{1}$$

where $\boldsymbol{b}$ is a mass-specific force density. They must hold globally for an RVE Ω,

$$\int_\Omega \boldsymbol{\sigma} \cdot \nabla \mathrm{d}V = \int_\Omega \rho(\ddot{\boldsymbol{x}} - \boldsymbol{b}) \, \mathrm{d}V, \qquad \int_\Omega (\boldsymbol{\sigma} - \boldsymbol{\sigma}^T) \, \mathrm{d}V = \boldsymbol{0}, \tag{2}$$

where the global balance of linear momentum may be transformed by Gauss' theorem and Cauchy's theorem $\boldsymbol{t} = \boldsymbol{\sigma} \cdot \boldsymbol{n}$,

$$\int_{\partial\Omega} \boldsymbol{t} \mathrm{d}A - \int_\Omega \rho(\ddot{\boldsymbol{x}} - \boldsymbol{b}) \, \mathrm{d}V = \boldsymbol{0}. \tag{3}$$

However, the incorporation of inertia and body forces leads to material laws which depend on superimposed rigid body motions.[1] Thus, we may consider only the static balance of linear momentum without body forces when using the RVE method.[2]

2.3. Micro–Macro-coupling

The micro–macro-coupling is obtained by assigning macroscale quantities to unweighted volume averages of the corresponding microscale quantities, where the integral is carried out over the domain occupied by the material. Thus, porous materials require either a treatment of pores by some material law, or need to be excluded from the volume integral. In the latter case, care must be taken when Gauss's theorem is applied. Here we exclude this peculiarities, assuming a space-filling arrangement of microconstituents. Following Nemat-Nasser [33], *"there is an inherent arbitrariness in the selection of suitable kinematic and dynamical quantities whose overall measures are defined in terms of unweighted volume averages of the corresponding micromeasure"*. To avoid ambiguities, it must be clarified which quantities are used. For several reasons it is advantageous to use the deformation gradient and the first Piola–Kirchhoff stresses,

$$\overline{\boldsymbol{F}} := \langle \boldsymbol{F} \rangle, \qquad \overline{\boldsymbol{T}} := \langle \boldsymbol{T} \rangle. \tag{4}$$

Firstly, $\overline{\boldsymbol{F}}$ and $\overline{\boldsymbol{T}}$ can be defined in terms of surface integrals in the reference placement,

$$\langle \boldsymbol{F} \rangle = \frac{1}{V_0} \int_{\Omega_0} \boldsymbol{x} \otimes \nabla_0 \mathrm{d}V = \frac{1}{V_0} \int_{\partial\Omega_0} \boldsymbol{x} \otimes \boldsymbol{n}_0 \mathrm{d}A, \tag{5}$$

$$\langle \boldsymbol{T} \rangle = \frac{1}{V_0} \int_{\partial\Omega_0} \boldsymbol{t} \otimes \boldsymbol{x}_0 \mathrm{d}A. \tag{6}$$

Relation (5) involves merely Gauss' theorem, while the latter relation is confirmed by reformulating with Cauchy theorem $\boldsymbol{t} = \boldsymbol{T} \cdot \boldsymbol{n}_0$, Gauss' theorem, and the static equilibrium condition without body forces $\boldsymbol{T} \cdot \nabla_0 = \boldsymbol{0}$ (see Section 2.2),

$$\begin{aligned} \langle \boldsymbol{T} \rangle &= \frac{1}{V_0} \int_{\partial\Omega_0} \boldsymbol{t} \otimes \boldsymbol{x}_0 \ \mathrm{d}A = \frac{1}{V_0} \int_{\partial\Omega_0} \boldsymbol{n}_0 \cdot (\boldsymbol{T}^T \otimes \boldsymbol{x}_0) \ \mathrm{d}A \qquad (7) \\ &= \frac{1}{V_0} \int_{\Omega_0} \nabla \cdot (\boldsymbol{T}^T \otimes \boldsymbol{x}_0) \ \mathrm{d}V = \frac{1}{V_0} \int_{\Omega_0} ((\boldsymbol{T} \cdot \nabla) \otimes \boldsymbol{x}_0 + \boldsymbol{T}) \ \mathrm{d}V \\ &= \frac{1}{V_0} \int_{\Omega_0} \boldsymbol{T} \ \mathrm{d}V. \qquad (8) \end{aligned}$$

Secondly, since the reference placement is time-independent, one can interchange the unweighted volume averaging and the material time derivative, i.e. $\dot{\overline{\boldsymbol{F}}} = \langle \dot{\boldsymbol{F}} \rangle = \langle \boldsymbol{F} \rangle^{\cdot} = \dot{\overline{\boldsymbol{F}}}$ and $\dot{\overline{\boldsymbol{T}}} = \langle \dot{\boldsymbol{T}} \rangle = \langle \boldsymbol{T} \rangle^{\cdot} = \dot{\overline{\boldsymbol{T}}}$.

Thirdly, $\boldsymbol{T}$ and $\dot{\boldsymbol{F}}$ are power-conjugate, which allows for a compact expression of the Hill–Mandel condition (Section 2.4). For the foregoing reasons, in this work $\boldsymbol{T}$ and $\boldsymbol{F}$ are taken for the micro–macro-coupling. Then, the macroscopic Cauchy stresses are obtained from $\bar{\boldsymbol{\sigma}} = \bar{J}^{-1} \overline{\boldsymbol{T}} \overline{\boldsymbol{F}}^T$, $\bar{J} = \det \overline{\boldsymbol{F}}$, which is not necessarily equivalent to $\langle \boldsymbol{\sigma} \rangle$. However, for the special case of the micro–macro-coupling in the first Piola–Kirchhoff stresses and the deformation gradient, it follows that $\bar{\boldsymbol{\tau}} = \langle \boldsymbol{\tau} \rangle$ [33].

[1] One can easily find examples which give an effective material behavior that violates the principle of invariance under superimposed rigid body motions [46]. Subject the RVE boundary to an accelerated rigid body motion and take $\overline{\boldsymbol{F}} := \langle \boldsymbol{F} \rangle$ and $\bar{\boldsymbol{\sigma}} := \langle \boldsymbol{\sigma} \rangle$ for the micro–macro-coupling to find that $\overline{\boldsymbol{F}} = \boldsymbol{I}$ holds constantly while $\overline{\boldsymbol{T}}$ depends on the motion.

[2] At this point, it is often argued that the volume integral $\left(\mathcal{O}\left(l_{\mathrm{mini}}^3\right)\right)$ is small compared to the surface integral $\left(\mathcal{O}\left(l_{\mathrm{mini}}^2\right)\right)$ due to the small size of the RVE, in order legitimate the disregard of inertia and body forces. This argument is conflicting with the idea of a possibly large RVE for a better representativity.

2.4. The Hill–Mandel condition

The Hill–Mandel condition, demands the equivalence of the stress power as perceived on the macroscale and on the microscale. For the small strain setting it is sufficient to consider

$$\langle \boldsymbol{\sigma} \cdot \cdot \dot{\boldsymbol{\varepsilon}} \rangle = \langle \boldsymbol{\sigma} \rangle \cdot \cdot \langle \dot{\boldsymbol{\varepsilon}} \rangle. \tag{9}$$

The latter equation is trivially satisfied if $\boldsymbol{\sigma}$ and $\dot{\boldsymbol{\varepsilon}}$ are homogeneous, from which the first interpretation of the Hill–Mandel-condition is derived: The larger the RVE is, the more homogeneous appears the material, i.e. the smaller are the fluctuations, leading to the conclusion that the Hill–Mandel-condition poses requirements on the RVE size [20].

However, the RVE is subjected to some boundary conditions. It was found that the Hill–Mandel-condition is satisfied for specific boundary data a priori [45], independent of the size of the RVE. From this, the second interpretation of the Hill–Mandel-condition arises: The boundary conditions should comply the Hill–Mandel-condition a priori to assure convergence to the effective material law with increasing RVE size. The latter interpretation appears to be widely accepted, since all commonly used boundary conditions a priori fulfill the Hill–Mandel-condition.

Before examining specific boundary conditions, the derivation of Suquet [45], which was originally given in the small strain setting, is reproduced here for the finite strain form of the Hill–Mandel-condition (see also Bertram [2]). The volume average of the volume-specific stress power of the RVE (left handside) must be equivalent to the volume-specific stress power on the macroscale,

$$\langle \boldsymbol{T} \cdot \cdot \dot{\boldsymbol{F}} \rangle = \overline{\boldsymbol{T}} \cdot \cdot \dot{\overline{\boldsymbol{F}}}. \tag{10}$$

Taking $\boldsymbol{F}$ and $\boldsymbol{T}$ for the micro–macro-coupling, the latter equation becomes

$$\langle \boldsymbol{T} \cdot \cdot \dot{\boldsymbol{F}} \rangle = \langle \boldsymbol{T} \rangle \cdot \cdot \langle \dot{\boldsymbol{F}} \rangle. \tag{11}$$

The latter equation can be recast with surface integrals, involving the boundary conditions. Up to Eq. (17), the dependency on $\boldsymbol{x}_0$ and t is written out, since the dependence is of importance for the argumentation. Firstly, the fluctuation part of $\dot{\boldsymbol{F}}$ is defined as

$$\tilde{\dot{\boldsymbol{F}}}(\boldsymbol{x}_0, t) := \dot{\boldsymbol{F}}(\boldsymbol{x}_0, t) - \dot{\overline{\boldsymbol{F}}}(t), \qquad \dot{\overline{\boldsymbol{F}}}(t) := \langle \dot{\boldsymbol{F}}(\boldsymbol{x}_0, t) \rangle. \tag{12}$$

Note that $\dot{\boldsymbol{F}}(\boldsymbol{x}_0, t) = \dot{\boldsymbol{H}}(\boldsymbol{x}_0, t)$, and consequently $\dot{\overline{\boldsymbol{F}}}(t) = \dot{\overline{\boldsymbol{H}}}(t)$ and $\tilde{\dot{\boldsymbol{F}}}(\boldsymbol{x}_0, t) = \tilde{\dot{\boldsymbol{H}}}(\boldsymbol{x}_0, t)$ hold. For the velocity field, one can define the decomposition

$$\dot{\boldsymbol{u}}(\boldsymbol{x}_0, t) := \dot{\boldsymbol{u}}(\boldsymbol{x}_0, t) - \dot{\overline{\boldsymbol{H}}}(t) \cdot \boldsymbol{x}_0, \dot{\boldsymbol{u}}(\boldsymbol{x}_0, t) - \dot{\overline{\boldsymbol{u}}}(\boldsymbol{x}_0, t). \tag{13}$$

Since $\boldsymbol{x}_0$ is not a function of t, the material time derivative and the material gradient $\otimes\nabla_0$ may be interchanged. Applying $\otimes\nabla_0$ to $\dot{\tilde{\boldsymbol{u}}}(\boldsymbol{x}_0, t)$ yields

$$\begin{aligned} \dot{\tilde{\boldsymbol{u}}}(\boldsymbol{x}_0, t) \otimes \nabla_0 &= \dot{\boldsymbol{u}}(\boldsymbol{x}_0, t) \otimes \nabla_0 - \dot{\overline{\boldsymbol{H}}}(t) = \dot{\boldsymbol{H}}(\boldsymbol{x}_0, t) - \dot{\overline{\boldsymbol{H}}}(t) \\ &= \tilde{\dot{\boldsymbol{H}}}(\boldsymbol{x}_0, t), \end{aligned} \tag{14}$$

i.e. $\dot{\tilde{\boldsymbol{u}}}(\boldsymbol{x}_0, t)$ and $\tilde{\dot{\boldsymbol{F}}}(\boldsymbol{x}_0, t)$ are related by

$$\tilde{\dot{\boldsymbol{F}}}(\boldsymbol{x}_0, t) = \dot{\tilde{\boldsymbol{u}}}(\boldsymbol{x}_0, t) \otimes \nabla_0. \tag{15}$$

Note that, unlike $\dot{\overline{\boldsymbol{F}}}(t)$, $\dot{\tilde{\boldsymbol{u}}}(\boldsymbol{x}_0, t)$ does depend on $\boldsymbol{x}_0$. The displacement $\tilde{\boldsymbol{u}}(\boldsymbol{x}_0, t)$ can be viewed as the part of the local displacement that stems from the homogeneous part $\overline{\boldsymbol{H}}$ of the displacement gradient. Although it depends linearly on $\boldsymbol{x}_0$ it is often referred to as the homogeneous part of the local displacement. Inserting the decomposition of $\dot{\boldsymbol{F}}(\boldsymbol{x}_0, t)$ into Eq. (11) yields

$$\langle \boldsymbol{T}(\boldsymbol{x}_0, t) \cdot \cdot \dot{\overline{\boldsymbol{F}}}(t) \rangle + \langle \boldsymbol{T}(\boldsymbol{x}_0, t) \cdot \cdot \tilde{\dot{\boldsymbol{F}}}(\boldsymbol{x}_0, t) \rangle = \langle \boldsymbol{T}(\boldsymbol{x}_0, t) \rangle \cdot \cdot \dot{\overline{\boldsymbol{F}}}(t), \tag{16}$$

where $\dot{\overline{\boldsymbol{F}}}(t)$ can be pulled out of the volume averaging, since it is independent on $\boldsymbol{x}_0$. Then one finds

$$\langle \boldsymbol{T}(\boldsymbol{x}_0,t)\cdot\cdot\dot{\widetilde{\boldsymbol{F}}}(\boldsymbol{x}_0,t)\rangle = 0. \tag{17}$$

One proceeds by using Eq. (15), and considering $\boldsymbol{T}\cdot\cdot(\dot{\tilde{\boldsymbol{u}}}\otimes\nabla_0)$ as one summand of a product rule,

$$\boldsymbol{T}\cdot\cdot\dot{\tilde{\boldsymbol{u}}}\otimes\nabla_0 + (\boldsymbol{T}\cdot\nabla_0)\cdot\dot{\tilde{\boldsymbol{u}}} = (\dot{\tilde{\boldsymbol{u}}}\cdot\boldsymbol{T})\cdot\nabla_0, \tag{18}$$

which allows to write

$$0 = \langle(\dot{\tilde{\boldsymbol{u}}}\cdot\boldsymbol{T})\cdot\nabla_0 - (\boldsymbol{T}\cdot\nabla_0)\cdot\dot{\tilde{\boldsymbol{u}}}\rangle. \tag{19}$$

Here one identifies $\boldsymbol{T}\cdot\nabla_0 = \boldsymbol{0}$ in the second summand as the local balance of linear momentum without inertia and body forces in the reference placement. Therefore, by considering only equilibrium states, this summand is dropped. The remaining summand is transformed by Gauss' theorem and Cauchy's theorem to

$$0 = \frac{1}{V_0}\int_{\partial\Omega_0}\dot{\tilde{\boldsymbol{u}}}\cdot\boldsymbol{T}\cdot\boldsymbol{n}_0\,\mathrm{d}A = \frac{1}{V_0}\int_{\partial\Omega_0}\dot{\tilde{\boldsymbol{u}}}\cdot\boldsymbol{t}\,\mathrm{d}A. \tag{20}$$

By this, the Hill–Mandel-condition is expressed as a surface integral in terms of the traction and displacement, which allows to examine specific boundary conditions with respect to the Hill–Mandel-condition.

3. Boundary conditions on the RVE

The boundary value problem is complete when at each surface point, with respect to a suitable orthogonal basis $\boldsymbol{b}_i$, either u_i, t_i or a mixture of both is prescribed. More general, the boundary conditions may be given implicitly in form of constraints, as it is the case for the periodic boundary conditions.

The boundary conditions to which an RVE may be subjected have been exhaustively discussed, see e.g. Suquet [45]. There are no natural or self-evident boundary conditions for the RVE, except for microstructures with a periodicity, where periodic boundary conditions are reasonable [31]. The most common boundary conditions are the homogeneous traction, linear displacement and periodic boundary conditions. Recent advances focus on the definition of boundary conditions which allow for an arbitrary localization of a RVE [7,36] (percolation path boundary conditions), where the periodic boundary conditions on a cubic RVE serve as the starting point. In this regard, a consideration of spherical RVEs with periodic boundary conditions is helpful. This topic is addressed in Section 8.

3.1. Uniform boundary data

The assumption of homogeneous tractions or linear displacements on the boundary are related to the Sachs/Reuss or Taylor/Voigt estimates, which assume a homogeneous stress or strain field not only on the boundary but in the entire volume. Thus, restricting this extreme assumptions to the RVE boundary gives estimates between these bounds. However, out of the commonly applied boundary conditions, homogeneous traction or linear displacement boundary conditions give bounds for the effective material law that may be obtained from a specific RVE [27,24]. While homogeneous traction boundary conditions give a softer effective material response, the linear displacement boundary conditions overestimate the stresses. In both cases, the Hill–Mandel-condition holds a priori, irrespective of the material law and the RVE size. The uniform boundary conditions have the advantage of an easy implementation.

3.1.1. Linear displacement boundary conditions

These are also termed as uniform strain boundary conditions [45], homogeneous displacement boundary conditions [11], kinematic uniform boundary conditions [23]. Given the average displacement gradient $\dot{\overline{\boldsymbol{H}}}_{\text{impose}}$ at each instant t, the velocity of the boundary points is given by

$$\dot{\boldsymbol{u}} = \dot{\overline{\boldsymbol{H}}}_{\text{impose}}\boldsymbol{x}_0 \quad \text{on } \partial\Omega. \tag{21}$$

One notes that due to the decomposition (13), $\dot{\tilde{\boldsymbol{u}}} = \boldsymbol{0}$ at the boundary, which renders the Hill–Mandel-condition (Eq. (20)) satisfied. The linear displacement boundary conditions correspond to the extremal Taylor and Voigt assumptions.

3.1.2. Homogeneous traction boundary conditions

Given the average stress tensor $\overline{\boldsymbol{T}}_{\text{impose}}$, the surface tractions are prescribed by

$$\boldsymbol{t} = \overline{\boldsymbol{T}}_{\text{impose}}\boldsymbol{n}_0 \qquad \text{on } \partial\Omega. \tag{22}$$

If this is inserted into the Hill–Mandel-condition (Eq. (20)), one notes that $\overline{\boldsymbol{T}}_{\text{impose}}$ can be pulled out of the integral, which leaves

$$0 = \frac{1}{V_0}\overline{\boldsymbol{T}}_{\text{impose}}\cdot\cdot\int_{\partial\Omega_0}\dot{\tilde{\boldsymbol{u}}}\otimes\boldsymbol{n}_0\mathrm{d}A = \frac{1}{V_0}\overline{\boldsymbol{T}}_{\text{impose}}\cdot\cdot\langle\dot{\widetilde{\boldsymbol{F}}}\rangle. \tag{23}$$

With $\langle\dot{\widetilde{\boldsymbol{F}}}\rangle = \boldsymbol{0}$ (Eq. (12)) one notes that the Hill–Mandel-condition is satisfied. The homogeneous traction boundary conditions correspond to the extremal Sachs and Reuss assumptions.

Commonly, material laws are formulated such that the stresses are a function of the motion of the body, although an inversion or even an implicit form is possible [40]. In case of the homogeneous traction boundary conditions, one prescribes the average stress state and obtains the average straining, i.e. it is the other way around. Miehe [31] used Lagrangian multipliers for changing the independent variable from $\boldsymbol{T}$ to $\boldsymbol{H}$. One finds that

$$\dot{\overline{\boldsymbol{H}}}_{\text{impose}} = \frac{1}{V_0}\int_{\partial\Omega_0}\dot{\boldsymbol{u}}\otimes\boldsymbol{n}_0\,\mathrm{d}A, \tag{24}$$

needs to be enforced, instead of Eq. (22). The latter is often termed as kinematic minimal boundary conditions [28], natural boundary conditions [10], weakly enforced kinematic boundary conditions [11] or static uniform boundary conditions [23]. The equivalence of the kinematic minimal boundary conditions to the homogeneous traction boundary conditions can be seen by considering perturbations of a solution of a boundary value problem with kinematic minimal boundary conditions. Suppose that we have imposed $\dot{\overline{\boldsymbol{H}}}_{\text{impose}}$ by Eq. (24), and found a global velocity field $\dot{\boldsymbol{u}}$ which we consider the solution. According to the incremental work minimization principle [37], the stress power attains a minimum state in equilibrium, thus any deviation from this solution must result in an increase of the incremental condensed potential. We denote an infinitesimal deviation from $\dot{\boldsymbol{u}}$ by $\delta\dot{\boldsymbol{u}}$. $\delta\dot{\boldsymbol{u}}$ must be compatible to the boundary conditions, i.e.,

$$\int_{\partial\Omega_0}\delta\dot{\boldsymbol{u}}\otimes\boldsymbol{n}_0\,\mathrm{d}A = \boldsymbol{0}. \tag{25}$$

The stress power change due to $\delta\dot{\boldsymbol{u}}$ is denoted as

$$\delta\dot{w} = \int_{\partial\Omega_0}\boldsymbol{t}\cdot\delta\dot{\boldsymbol{u}}\,\mathrm{d}A. \tag{26}$$

The tractions $\boldsymbol{t}$ can be decomposed into a homogeneous and a fluctuation part,

$$\boldsymbol{t} = \overline{\boldsymbol{T}}\cdot\boldsymbol{n}_0 + \tilde{\boldsymbol{t}}, \qquad \int_{\partial\Omega_0}\tilde{\boldsymbol{t}}\otimes\boldsymbol{n}_0\,\mathrm{d}A = \boldsymbol{0}. \tag{27}$$

We insert this decomposition into the variation of the stress power,

$$\delta\dot{w} = \int_{\partial\Omega_0} (\overline{\boldsymbol{T}} \cdot \boldsymbol{n}_0 + \tilde{\boldsymbol{t}}) \cdot \delta\dot{\boldsymbol{u}} \, \mathrm{d}A \tag{28}$$

$$= \int_{\partial\Omega_0} (\overline{\boldsymbol{T}} \cdot \cdot \, \delta\dot{\boldsymbol{u}} \otimes \boldsymbol{n}_0 + \tilde{\boldsymbol{t}} \cdot \delta\dot{\boldsymbol{u}}) \, \mathrm{d}A. \tag{29}$$

The first summand is zero by definition: We can pull out $\overline{\boldsymbol{T}}$, and the remaining integral is equal to Eq. (25). It remains

$$\delta\dot{w} = \int_{\partial\Omega_0} \tilde{\boldsymbol{t}} \cdot \delta\dot{\boldsymbol{u}} \, \mathrm{d}A. \tag{30}$$

One can see that $\tilde{\boldsymbol{t}} = \boldsymbol{0}$ must hold if $\dot{\boldsymbol{u}}$ is a minimizer of $\dot{w}$. Otherwise it is possible to reduce the stress power by choosing $\delta\dot{\boldsymbol{u}} = \alpha\tilde{\boldsymbol{t}}$, with $\alpha < 0$ (and the corresponding physical unit). This is admissible because of Eq. (27) being in accordance with Eq. (25). Thus, $\delta\dot{w}$ can only be zero for all admissible perturbations of $\dot{\boldsymbol{u}}$ if $\tilde{\boldsymbol{t}} = \boldsymbol{0}$, i.e. the solution in case of kinematic minimal boundary conditions must correspond to a state of homogeneous tractions, as prescribed by the homogeneous traction boundary conditions.

3.2. Mixing of homogeneous traction and linear displacement boundary conditions

Since the linear displacement boundary conditions and homogeneous traction boundary conditions pose bounds, these boundary conditions are sometimes mixed on one RVE, in order to get a better approximation of the real material behavior [25,14]. Two different approaches are possible.

3.2.1. Globally mixed boundary conditions

One may prescribe on all surface points mixed boundary conditions, where with respect to a suitable orthogonal basis a mixture of the components u_i and t_i is prescribed, which are obtained from uniform $\overline{\boldsymbol{H}}_{\text{impose}}\boldsymbol{x}_0$ and $\overline{\boldsymbol{T}}_{\text{impose}}\boldsymbol{x}_0$. For this case the Hill–Mandel-condition holds a priori [19]. This can be seen by decomposing

$$\dot{\boldsymbol{u}} = \dot{\boldsymbol{u}}_{\text{impose}} + \dot{\boldsymbol{u}}_{\text{reaction}} \tag{31}$$

$$\boldsymbol{t} = \boldsymbol{t}_{\text{impose}} + \boldsymbol{t}_{\text{reaction}}, \tag{32}$$

where the relations

$$0 = \dot{\boldsymbol{u}}_{\text{impose}} \cdot \boldsymbol{t}_{\text{impose}} \tag{33}$$

$$0 = \dot{\boldsymbol{u}}_{\text{reaction}} \cdot \boldsymbol{t}_{\text{reaction}} \tag{34}$$

$$0 = \dot{\boldsymbol{u}}_{\text{reaction}} \cdot \dot{\boldsymbol{u}}_{\text{impose}} \tag{35}$$

$$0 = \boldsymbol{t}_{\text{reaction}} \cdot \boldsymbol{t}_{\text{impose}} \tag{36}$$

must hold. With $\dot{\boldsymbol{u}}_{\text{impose}} = \dot{\overline{\boldsymbol{H}}}_{\text{impose}}\boldsymbol{x}_0$ it is clear that $\dot{\boldsymbol{u}}_{\text{impose}}$ does not contribute to $\dot{\tilde{\boldsymbol{u}}}$, i.e.,

$$\dot{\tilde{\boldsymbol{u}}} \cdot \dot{\boldsymbol{u}}_{\text{impose}} = 0, \tag{37}$$

which leads to the conclusion that $\dot{\tilde{\boldsymbol{u}}}$ must be parallel to $\dot{\boldsymbol{u}}_{\text{reaction}}$. Examining the Hill–Mandel-condition leads to

$$0 = \frac{1}{V_0}\int_{\partial\Omega_0} \dot{\tilde{\boldsymbol{u}}} \cdot \boldsymbol{t} \, \mathrm{d}A = \frac{1}{V_0}\int_{\partial\Omega_0} (\dot{\tilde{\boldsymbol{u}}} \cdot \boldsymbol{t}_{\text{impose}} + \dot{\tilde{\boldsymbol{u}}} \cdot \boldsymbol{t}_{\text{reaction}}) \, \mathrm{d}A. \tag{38}$$

Since $\dot{\tilde{\boldsymbol{u}}}$ is parallel to $\dot{\boldsymbol{u}}_{\text{reaction}}$ and due to Eq. (34) the second summand vanishes, and the remainder corresponds to Eq. (23), i.e., the Hill–Mandel-condition is met a priori.

3.2.2. Locally pure homogeneous tractions and linear displacements

Another possibility is to divide the surface into the parts $\partial\Omega_{\boldsymbol{u}}$ and $\partial\Omega_{\boldsymbol{t}}$ where $\dot{\boldsymbol{u}} = \dot{\overline{\boldsymbol{H}}}_{\text{impose}}\boldsymbol{x}_0$ and $\boldsymbol{t} = \overline{\boldsymbol{T}}_{\text{impose}}\boldsymbol{n}_0$ are prescribed, respectively. Then the Hill–Mandel-condition gives (Eq. (20))

$$0 = \frac{1}{V_0}\int_{\partial\Omega_{0\boldsymbol{u}}} [(\dot{\overline{\boldsymbol{H}}}_{\text{impose}} - \dot{\overline{\boldsymbol{H}}})\boldsymbol{x}_0] \cdot [\boldsymbol{T}\boldsymbol{n}_0] \, \mathrm{d}A + \frac{1}{V_0}\int_{\partial\Omega_{0\boldsymbol{t}}} [(\dot{\boldsymbol{H}} - \dot{\overline{\boldsymbol{H}}})\boldsymbol{x}_0] \cdot [\overline{\boldsymbol{T}}_{\text{impose}}\boldsymbol{n}_0] \, \mathrm{d}A. \tag{39}$$

with $\dot{\tilde{\boldsymbol{u}}} = \dot{\boldsymbol{u}} - \dot{\overline{\boldsymbol{H}}}\boldsymbol{x}_0$. Unfortunately, it appears that no constraints can be given that ensure the Hill–Mandel-condition a priori.

3.3. Periodic boundary conditions

The periodic boundary conditions are a compromise between the homogeneous traction boundary conditions and linear displacement boundary conditions in the sense that they distribute the constraints that are needed to complete the boundary value problem equally on $\boldsymbol{t}$ and $\boldsymbol{u}$. The periodic boundary conditions also result in a better convergence to the effective material behavior as the RVE size is increased, which is why they are mostly preferred to the homogeneous traction boundary conditions and the linear displacement boundary conditions. In order to apply the periodic boundary conditions, one needs to form pairs $\boldsymbol{x}_0^+$ and $\boldsymbol{x}_0^-$ of all boundary points, where

$$\boldsymbol{n}_0^+ = -\boldsymbol{n}_0^- \tag{40}$$

must hold. This can be done in a reasonable fashion if the RVE-shape allows to fill the space without gaps by a periodic arrangement of equal RVEs. For 3D problems, mostly cuboid-shaped RVE are used. Regarding the FE method, this is mostly done by a similar node arrangement on opposing surfaces of the RVE, although this restriction can be surmounted [34]. Then, by assigning opposing boundary points to pairs, and enforcing periodic boundary conditions, the principle of sections holds for the opposing RVE surfaces. For homogeneous traction boundary conditions and linear displacement boundary conditions, opposing surfaces are in force equilibrium or kinematically compatible, respectively. This renders the periodic boundary conditions most suitable for periodic microstructures, where it may be sufficient to consider only the smallest possible repeatable unit cell. Given the pairs $\boldsymbol{x}_0^{\pm}$ with $\boldsymbol{n}_0^+ = -\boldsymbol{n}_0^-$ and an imposed average displacement gradient $\dot{\overline{\boldsymbol{H}}}_{\text{impose}}$, the periodic boundary conditions are

$$\dot{\boldsymbol{u}}^+ - \dot{\boldsymbol{u}}^- = \dot{\overline{\boldsymbol{H}}}_{\text{impose}}(\boldsymbol{x}_0^+ - \boldsymbol{x}_0^-) \tag{41}$$

$$\boldsymbol{t}^+ - \boldsymbol{t}^- = \boldsymbol{0}, \tag{42}$$

which are six implicit equations for six degrees of freedom (three on the two surface points $\boldsymbol{x}^{\pm}$), necessary to complete the mixed boundary value problem. Only if $\boldsymbol{n}_0^+ = -\boldsymbol{n}_0^-$ we find that $\dot{\overline{\boldsymbol{H}}}_{\text{impose}} = \dot{\overline{\boldsymbol{H}}}$, which is needed for the verification of the Hill–Mandel-condition. $\overline{\boldsymbol{H}}$ is given by Eq. (24). Splitting the surface integral into the minus- and plus-part and using $\boldsymbol{n}_0^+ = -\boldsymbol{n}_0^-$ gives

$$\dot{\overline{\boldsymbol{H}}} = \frac{1}{V_0}\int_{\partial\Omega_0^+} \dot{\boldsymbol{u}}^+ \otimes \boldsymbol{n}_0^+ \, \mathrm{d}A + \frac{1}{V_0}\int_{\partial\Omega_0^-} \dot{\boldsymbol{u}}^- \otimes \boldsymbol{n}_0^- \, \mathrm{d}A \tag{43}$$

$$= \frac{1}{V_0}\int_{\partial\Omega_0^+} (\dot{\boldsymbol{u}}^+ - \dot{\boldsymbol{u}}^-) \otimes \boldsymbol{n}_0^+ \, \mathrm{d}A \tag{44}$$

$$= \frac{1}{V_0}\int_{\partial\Omega_0^+} \dot{\overline{\boldsymbol{H}}}_{\text{impose}}(\boldsymbol{x}_0^+ - \boldsymbol{x}_0^-) \otimes \boldsymbol{n}_0^+ \, \mathrm{d}A \tag{45}$$

$$= \frac{1}{V_0}\dot{\overline{\boldsymbol{H}}}_{\text{impose}}\int_{\partial\Omega_0} \boldsymbol{x}_0 \otimes \boldsymbol{n}_0 \, \mathrm{d}A = \dot{\overline{\boldsymbol{H}}}_{\text{impose}}. \tag{46}$$

For the periodic boundary conditions, the Hill–Mandel-condition holds as well a priori: By subtracting Eq. (13) for the minus-side from the plus-side we obtain

$$\dot{\boldsymbol{u}}^+ - \dot{\boldsymbol{u}}^- = \dot{\overline{\boldsymbol{H}}} \cdot (\boldsymbol{x}_0^+ - \boldsymbol{x}_0^-) + \dot{\tilde{\boldsymbol{u}}}^+ - \dot{\tilde{\boldsymbol{u}}}^-. \tag{47}$$

Given that $\dot{\bar{\boldsymbol{H}}}_{\text{impose}} = \dot{\bar{\boldsymbol{H}}}$, we can use Eq. (41) to summarize to

$$\dot{\boldsymbol{u}}^{+} = \dot{\boldsymbol{u}}^{-}. \tag{48}$$

Then, together with Eq. (42), the Hill–Mandel-condition (Eq. (20)) must hold, since opposing surface points mutually cancel out their contribution to the surface integral.

4. The shape of the RVE

4.1. Non-periodic microstructures

In the case of non-periodic microstructures, the homogenized material response must be approximated by considering possibly large RVE. As the size of the RVE increases, the representativity gets better, and the surface-to-volume ratio tends to zero. Presuming that there is no softening or fracture or other localization-inducing material behavior, the influence of the boundary conditions vanishes (see Section 8).

Considering that the boundary influence is artificial, and therefore preferably small right from the start, spherical RVE appear advantageous. Compared to a cubical RVE of the same volume, one has 19.4% less surface. It is therefore to expect that the spherical RVEs perform better than cubical RVEs.

While one might accept the use of spherical RVE with uniform boundary conditions, the use of periodic boundary conditions on spherical RVE appears prohibitive at first glance. However, the application of periodic boundary conditions is advantageous due to the better convergence. Thus, the periodic boundary conditions are also applied in case of non-periodic microstructures, mostly with cuboid-shaped RVE and periodic microstructures, which motivates their name. However, this periodicity is artificial. It is in fact not necessary to insist on periodically repeatable unit cells. The periodic boundary conditions require merely that the paired surface points have opposing surface normals in the reference placement. The argument that the RVE must have a shape that allows for a complete filling of the space does not enter as an equation. It is merely used to facilitate the assignment of pairs of surface points with opposing surface normals. It is therefore possible to use the periodic boundary conditions with non-periodic volume cells like spheres or ellipsoids, as long as the assignment of pairs of surface points complies with $\boldsymbol{n}_0^{+} = -\boldsymbol{n}_0^{-}$. Of course, the term "periodic" is misleading when the periodic boundary conditions are applied to non-periodic shapes. In that case, it might be better to speak of coupled boundary conditions, although not the boundary conditions itself but the shape of the RVE differs. Thus, we continue to refer to periodic boundary conditions, even if applied to a sphere.

It is worth noting that this assignment of pairs is, in contrast to cubical RVEs, unique for spherical RVEs. However, in contrast to the periodically repeatable unit cells, the opposing surface normals $\boldsymbol{n}^{\pm}$ of arbitrarily shaped RVEs need not remain parallel during the deformation. This has, nonetheless, no effect at all for the argumentation, which is based entirely on $\boldsymbol{n}_0$.

4.2. Periodic microstructures

If the microstructure under consideration is periodic, one can construct arbitrary large material samples from an irreducible unit cell. For many cases, it is sufficient to consider a periodically repeatable unit cell with periodic boundary conditions. Only for some cases this is not sufficient, e.g., if one wants to associate structural instabilities of the RVE with material instabilities of the effective material [32]. Then, one takes a larger, periodically repeatable material section as RVE. In summary, the use of non-periodic RVE shapes is reasonable only in case of non-periodic microstructures.

5. Material and simulation setup

5.1. Material behavior of the matrix and inclusions

The material under consideration is a matrix–inclusion material. The matrix is an isotropic, linearly elastic, perfect plastic von Mises material without hardening. The inclusions with a total volume fraction of 0.3 are spherical, isotropic, linearly elastic particles of equal diameter, distributed uniformly without preferred alignment or pattern. They are considerably stiffer than the matrix material. The material parameters are collected in Table 1.

5.2. Definition of the RVE

The calculations have been carried out using the FE system ABAQUS, which has a Python interface. We created a Python script that reads an input file, from which the FE-model of the RVE is created. The input file contains information regarding the desired shape of the RVE, the material properties, the inclusion volume fraction, the boundary conditions, the element type and the average displacement gradient. The mesh has been generated such that each surface node had an antipode, in order to allow for an easy application of periodic boundary conditions. The meshing has not been adapted to the matrix-inclusion interfaces, i.e., the material assignment is not element-wise, but on the integration point level. The material assignment has been obtained by generating a large cubic sample of the material with randomly located spherical inclusions, with a total volume fraction of 0.3. The inclusions have been generated without intersections. Out of this material section we generated many RVE by randomly assigning the RVE mid-point. Consequently, no periodicity has been introduced by the inclusion distribution. From these RVE we selected the ones which best recovered the inclusion volume fraction, with a maximum absolute deviation of 0.005 from the desired 0.3. The RVE-sizes have been scaled by setting the RVE diameter (spherical RVE) or edge length (cubical RVE) to integer multiples (namely 1, 2, 3, 4, 5) of the inclusion diameter, resulting in the RVE sizes given in Table 2. We maintained a minimum elements-per-inclusion ratio of ≈270 for the purely elastic and of ≈900 for the elastoplastic simulations, using 8-node hexahedral elements with linear shape functions (C3D8) (Fig. 1). No special treatment, like the generation of a periodic microstructure, has been employed for the cubical RVE with periodic boundary conditions.

Table 1
Material parameter for the matrix and the inclusion material.

Parameter	Matrix	Inclusion
Young's modulus E in MPa	5000	50,000
Poisson's ratio ν	0.4	0.3
Flow stress σ_f in MPa	10	–
Volume fraction	0.7	0.3

Table 2
Number of configurations for the different combinations of shape, boundary conditions and size. The volumes of the cubical RVEs differ by a factor of $6/\pi$ from the corresponding spherical RVEs.

$V_{\text{RVE}}/V_{\text{inc}}$	PBC	LDBC	HTBC	$V_{\text{RVE}}/V_{\text{inc}}$	PBC	LDBC	HTBC
1.91	10	10	10	1	10	10	10
15.28	10	10	10	8	10	10	10
51.57	10	10	–	27	10	10	10
122.23	10	10	–	64	10	10	–
238.73	10	10	–	125	10	10	–
Cubical RVE				Spherical RVE			

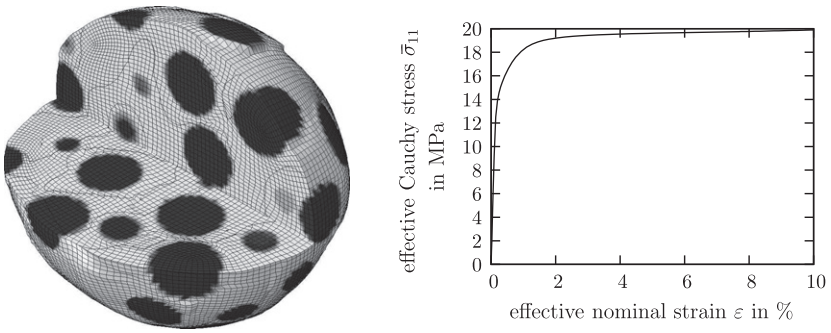

Fig. 1. Deformed spherical RVE with periodic boundary conditions (left), typical effective stress-strain curve (right).

5.3. Incorporation of boundary conditions

For the application of the boundary conditions, three nodes that are not attached to the FE mesh have been created. The nine additional displacement degrees of freedom have been assigned to the components of the average displacement gradient. Then, the boundary conditions have been incorporated by constraint equations, by which the displacement degrees of freedom of the surface nodes are coupled by the discrete versions of Eqs. (21), linear displacement boundary conditions), ((24), homogeneous traction boundary conditions) and ((41) and (42), periodic boundary conditions) to the three additional nodes.

While the linear displacement boundary conditions and the periodic boundary conditions are incorporated relatively simple, the homogeneous traction boundary conditions posed some problems. These have been implemented via the kinematic minimal boundary conditions by constraining the displacements according to the discrete version of Eq. (24). The latter equation involves weight factors that assign an area fraction to the surface nodes, which needed to be determined. This problem has been solved by carrying out a FE simulation of the homogeneous, isotropic elastic RVE, where a small volume change was imposed. The weight factors have been calculated from the absolute values of the resulting surface nodal forces. Secondly, the constraint equations require a careful implementation, due to the appearance of the same degree of freedom in more than one equation and the way that ABAQUS handles constraint equations. The first degree of freedom of an equation cannot appear in a following equation, i.e. an according ordering is necessary. Finally, the resulting constraint equations (involving all surface nodes) are very long, which results in a drastic decrease of the performance of ABAQUS. This issue is discussed elsewhere [15]. For these reasons, one might consider the implementation of homogeneous tractions via the kinematic minimal boundary conditions as unnecessary complicated. However, it is problematic to study the effect of different boundary conditions without expressing them with respect to the same independent variable, in our case $\overline{\boldsymbol{H}}$. Otherwise, one needs to identify iteratively a loading $\overline{\boldsymbol{T}}$ that yields the desired average deformation for every single boundary value problem, which results also in a drastic increase of computational effort. It should be noted that the troubles with long constraint equations are ABAQUS-specific, and efficient treatments for such special linear systems are at hand.[3]

[3] For example, the conjugate gradients method, in conjunction with a sparse matrix storage scheme that does not rely on a small bandwidth, or the substructure technique can be employed. Fritzen and Böhlke (2010), Technische Mechanik 30 (4), to be found at http://www.uni-magdeburg.de/ifme/zeitschrift_tm/2010_Heft4/05_Fritzen.html.

5.4. Extraction of the average stresses

Depending on whether one prescribes the displacements or the forces on the nine additional degrees of freedom, one can prescribe $\overline{\boldsymbol{H}}$, $\overline{\boldsymbol{T}}$ or a mixture of both, and extract the other one. For the extraction or prescription of the stresses, the reference volume of the RVE enters as a factor of proportionality.

6. Rate of convergence for spherical and cubical RVE

6.1. Simulation setup

For the study of convergence, we carried out uniaxial tension tests, in which the nominal strain ε is increased to 10%. The latter is accomplished by imposing

$$\overline{H}_{(\mathrm{uax})ij} = \begin{bmatrix} \varepsilon & 0 & 0 \\ 0 & - & 0 \\ 0 & 0 & - \end{bmatrix}. \tag{49}$$

Not prescribing $\overline{H}_{(\mathrm{uax})22}$ and $\overline{H}_{(\mathrm{uax})33}$ results in zero stress components $\overline{T}_{22}$ and $\overline{T}_{33}$. As characteristic quantities for the statistical evaluation, Young's modulus $E = \bar{\sigma}_{11}/\overline{H}_{11}$ at the onset of the deformation and the Cauchy stress $\bar{\sigma}_{11}$ at 10% of nominal strain have been extracted. Six combinations of RVE shapes and boundary conditions have been considered (cube and sphere with homogeneous traction boundary conditions, linear displacement boundary conditions and periodic boundary conditions). For any of these, at most five different RVE sizes have been taken into account. Then, 10 realizations with different inclusion distributions have been carried out for each of these combinations (see Table 2).

The homogeneous traction boundary conditions did not allow for large RVE sizes due to the inappropriate way that ABAQUS handles long constraint equations. This problem is mostly overcome by applying the homogeneous traction boundary conditions directly in terms of traction vectors, which, however, has the disadvantage that only $\overline{\boldsymbol{T}}$ can be prescribed. Also, the homogeneous traction boundary conditions allow for needle-like localizations [22], which renders them improper for simulations involving large plastic deformations. Thus, for the homogeneous traction boundary conditions, we considered only Young's modulus for small RVE sizes.

6.2. Results

In Fig. 1, a typical stress–strain curve of the macroscale material is depicted, in Fig. 2 the deformed shape with a color map of the equivalent plastic strain is depicted. One can see the onset of

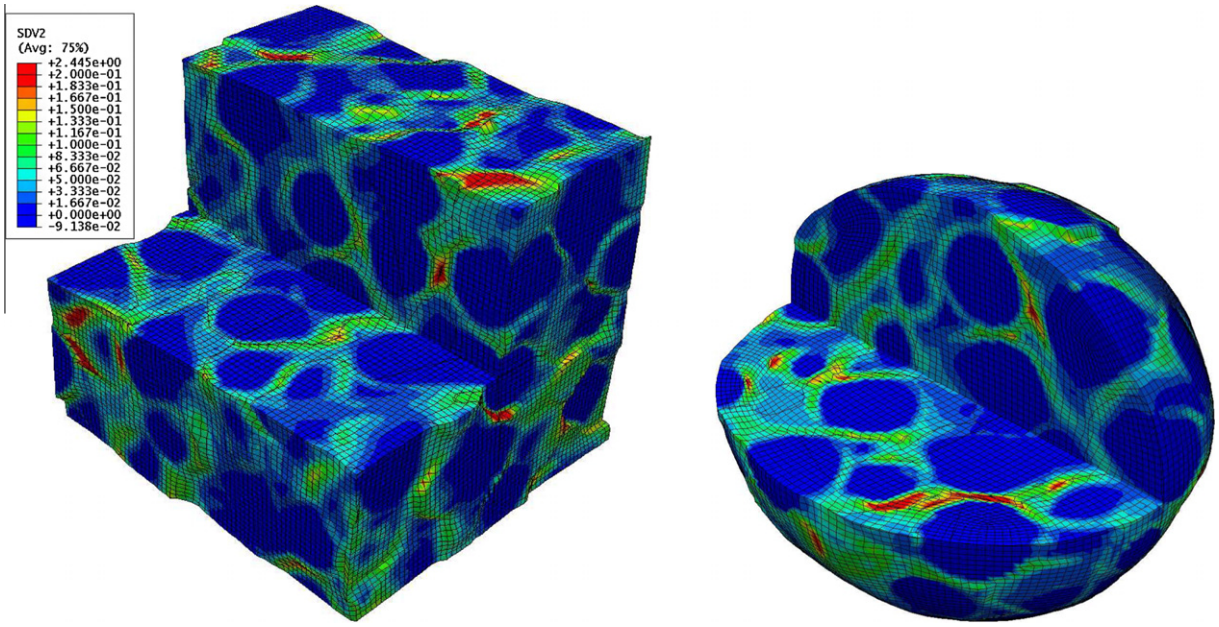

Fig. 2. Deformed cubical and spherical RVE with periodic boundary conditions ($\frac{1}{4}$ cut out). The coloring indicates the equivalent plastic strain from 0 (blue) to 0.2 (red). (For interpretation of the references to color in this figure legend, the reader is referred to the web version of this article.)

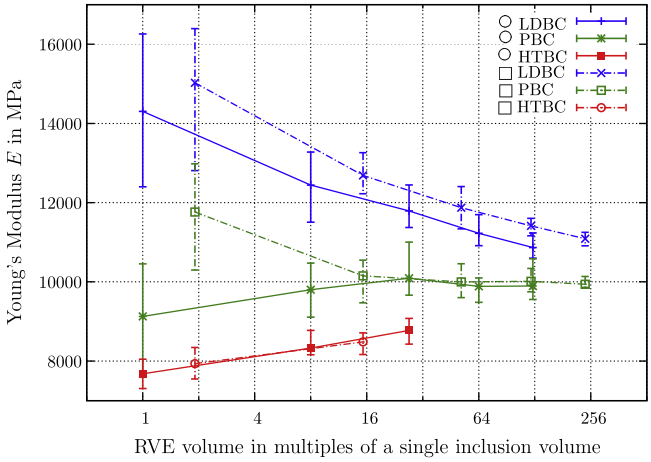

Fig. 3. Convergence of Young's modulus, ensemble min, max and average.

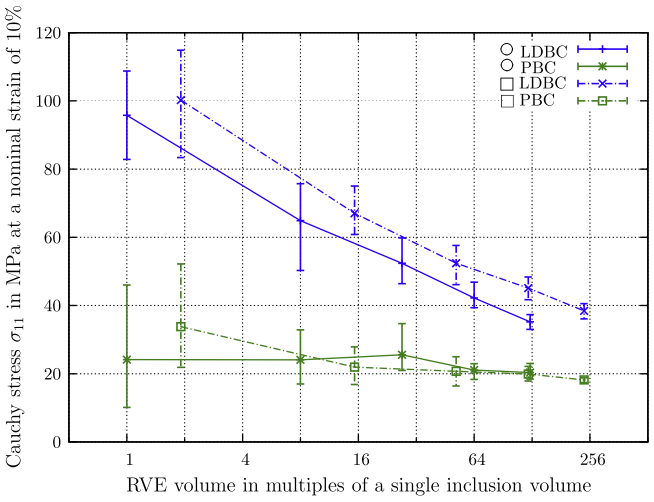

Fig. 4. Convergence of σ_{11} at 10% of nominal strain, ensemble min, max, and average.

plastic flow[4] at $\bar{\sigma}_{11} \approx 12$ MPa, followed by a short stage of effective hardening, before a value of approximately $\bar{\sigma}_{11} = 20$ MPa is approached asymptotically. Unlike the individual microscale materials, the effective material does not exhibit a sharp, but a rather smooth transition from the elastic to the plastic behavior. This is due to the inhomogeneous formation (first deviation from the linear elastic behavior) and growth (stage of effective hardening) of the plastic zones displayed in Fig. 2. The qualitative distinct behavior of the effective material is a result of the microscale-constituents interaction, see e.g. Chawla and Shen [6], who refer to the described behavior as "apparent work hardening".

The results for Young's modulus at $\varepsilon = 0$ and $\bar{\sigma}_{11}$ at $\varepsilon = 10\%$ for the different RVE sizes and boundary conditions is depicted in Figs. 3 and 4. Young's modulus tends to approximately 10 GPa, which is well inside the Reuss-Voigt (6849.3 – 18674.4 MPa) and Hashin–Shtrikman (8484.9 – 13912.1 MPa) bounds.

[4] Here, we locate the onset of effective plastic flow at $\frac{\partial \bar{\sigma}_{11}}{\partial \bar{\varepsilon}_{11}} = 0.5E$, with E being Youngs modulus.

As these figures indicate, the convergence behavior is similar both for the elastic and the plastic properties. In both cases, the results with periodic boundary conditions converge fastest, while the linear displacement boundary conditions predict a stiffer and the homogeneous traction boundary conditions a softer material behavior. Also, there is a gain in the rate of convergence for the spherical RVEs over the cubical RVEs, most notable for the linear displacement boundary conditions: to obtain similar results, one needs cubical RVEs with a volume approximately two to three times that of the corresponding spherical RVEs. This tendency is also observed for the periodic boundary conditions, though less pronounced. Interestingly, the effective Young's modulus displays no systematic difference between spherical and cubical RVE with homogeneous traction boundary conditions.

The graph given by Kanit et al. [23] (Fig. 7) displays a wider scattering compared to our findings. This is due to considering only

RVEs with inclusion volume fractions close to the macroscopic one in this work (see Section 5.2). Therefore, we have a reduced scattering in general. From that it became apparent that the homogeneous traction boundary conditions display a considerably weaker scattering for small RVE sizes than the periodic boundary conditions and linear displacement boundary conditions, independently of the shape of the RVE. For the smallest sphere we have a relative difference $(x_{\max} - x_{\min})/x_{\min}$ that is approximately three to four times smaller than for the periodic boundary conditions and linear displacement boundary conditions (0.101 (HTBC) vs 0.311 (LDBC) and 0.378 (PBC)), while for the smallest cube this difference is slightly less pronounced (0.106 (HTBC) vs 0.28 (LDBC) and 0.26 (PBC)), due to the smaller volume of the sphere.

7. Quantification of the shape-induced anisotropy

The shape-induced elastic anisotropy is determined by imposing mutually orthogonal small strains,

$$\overline{H}_{(1)ij} = \begin{bmatrix} \delta & 0 & 0 \\ 0 & 0 & 0 \\ 0 & 0 & 0 \end{bmatrix}, \quad \overline{H}_{(2)ij} = \begin{bmatrix} 0 & 0 & 0 \\ 0 & \delta & 0 \\ 0 & 0 & 0 \end{bmatrix}, \quad \overline{H}_{(3)ij} = \begin{bmatrix} 0 & 0 & 0 \\ 0 & 0 & 0 \\ 0 & 0 & \delta \end{bmatrix}, \tag{50}$$

$$\overline{H}_{(4)ij} = \begin{bmatrix} 0 & \delta & 0 \\ \delta & 0 & 0 \\ 0 & 0 & 0 \end{bmatrix}, \quad \overline{H}_{(5)ij} = \begin{bmatrix} 0 & 0 & \delta \\ 0 & 0 & 0 \\ \delta & 0 & 0 \end{bmatrix}, \quad \overline{H}_{(6)ij} = \begin{bmatrix} 0 & 0 & 0 \\ 0 & 0 & \delta \\ 0 & \delta & 0 \end{bmatrix}. \tag{51}$$

where δ is small enough to guarantee a purely elastic material response. The components of the stiffness tetrad are then obtained by

$$C_{ij11} = \bar{\sigma}_{ij}/\delta \quad \text{imposing } \boldsymbol{H}_{(1)}, \tag{52}$$
$$C_{ij22} = \bar{\sigma}_{ij}/\delta \quad \text{imposing } \boldsymbol{H}_{(2)}, \tag{53}$$
$$C_{ij33} = \bar{\sigma}_{ij}/\delta \quad \text{imposing } \boldsymbol{H}_{(3)}, \tag{54}$$
$$C_{ij12} = C_{ij21} = \bar{\sigma}_{ij}/\delta \quad \text{imposing } \boldsymbol{H}_{(4)}, \tag{55}$$
$$C_{ij13} = C_{ij31} = \bar{\sigma}_{ij}/\delta \quad \text{imposing } \boldsymbol{H}_{(5)}, \tag{56}$$
$$C_{ij23} = C_{ij32} = \bar{\sigma}_{ij}/\delta \quad \text{imposing } \boldsymbol{H}_{(6)}. \tag{57}$$

Any deviation from elastic isotropy must stem from the RVE itself, since the effective material under consideration is isotropic. We examined five RVE sizes (see Table 2), where the periodic boundary conditions have been used on spherical and cubical RVE. For each model we examined 100 different configurations of the microstructure, of which we extracted the average stiffness tetrad. The latter is weakly anisotropic. The overall anisotropy is quantified by the anisotropy measure a, given by

$$a = \|\mathbb{D} - (\mathbb{P}_1 \cdots \mathbb{D})\mathbb{P}_1 - \frac{1}{5}(\mathbb{P}_2 \cdots \mathbb{D})\mathbb{P}_2\| \tag{58}$$

$$\mathbb{D} = \frac{\ln(\det(\mathbb{C})^{-\frac{1}{6}}\mathbb{C})}{\|\ln(\det(\mathbb{C})^{-\frac{1}{6}}\mathbb{C})\|}, \tag{59}$$

with the first and second isotropic projectors $\mathbb{P}_1 = \frac{1}{3}\boldsymbol{I} \otimes \boldsymbol{I}$ and $\mathbb{P}_2 = \mathbb{I} - \mathbb{P}_1$. The factor 1/5 must be introduced to normalize $\mathbb{P}_2$. In the following, we restrict to symmetric fourth order tensors that map symmetric second order tensors into symmetric second order tensors. By this, we can extend the eigenvalue problem to this tensor space and define the inverse of $\mathbb{C}$ by restricting to positive definite tensors $\mathbb{C}$. The function $a(\mathbb{C})$ is constructed such that

$$a(\mathbb{C}) = a(\alpha\mathbb{C}), \quad \alpha \in \mathbb{R}, \quad \alpha > 0 \tag{60}$$
$$a(\mathbb{C}) = a(\mathbb{C}^{-1}) \tag{61}$$

hold, in order to make a independent of whether the anisotropy of the stiffness $\mathbb{C}$ or the compliance $\mathbb{C}^{-1}$ is evaluated, and to make a independent on the absolute values of the stiffness or compliance. The properties of $a(\mathbb{C})$ are examined in the Appendix. Likewise, we can filter out the cubic anisotropy by

$$a_c = \|\mathbb{D} - (\mathbb{P}_1 \cdots \mathbb{D})\mathbb{P}_1 - \frac{1}{2}(\mathbb{P}_{c2} \cdots \mathbb{D})\mathbb{P}_{c2} - \frac{1}{3}(\mathbb{P}_{c3} \cdots \mathbb{D})\mathbb{P}_{c3}\|, \tag{62}$$

with the cubic eigenprojectors $\mathbb{P}_{c2} = \mathbb{I} - \mathbb{P}_1 - \mathbb{P}_{c3}$ and $\mathbb{P}_{c3} = \sum_{i=1}^{3} \boldsymbol{d}_i \otimes \boldsymbol{d}_i \otimes \boldsymbol{d}_i \otimes \boldsymbol{d}_i$, where $\boldsymbol{d}_i$ is an orthonormal basis that coincides with the cubic anisotropy axes. Here, we presumed that $\boldsymbol{d}_i$ coincides with the edges of the cubical RVEs. Note that $a_c \leqslant a$ holds. Commonly, the cubic anisotropy is quantified by the Zener ratio [48],

$$Z = \frac{2C_{ijij}}{(C_{iiii} - C_{iijj})}, \tag{63}$$

presuming that the components of $\mathbb{C}$ are given with respect to $\boldsymbol{d}_i$. Then, the eigenvalues of a cubic stiffness tetrad are given by $\lambda_1 = C_{1111} + 2C_{1122}$, $\lambda_2 = C_{1111} - C_{1122}$ and $\lambda_3 = 2C_{1212}$ [3]. Thus, one can identify $Z = \lambda_3/\lambda_2$.

Comparing a and a_c, which differ only by the cubic part of the anisotropy that has been removed in a_c, shows that the anisotropy of the cubical RVE is indeed mostly cubic (Fig. 5), with $a/a_c \approx 5 - 10$. The largest anisotropy is encountered for the smallest cubical RVE with periodic boundary conditions, with $a = 0.198$, $a_c = 0.019$ and $Z = 0.765$. For the spherical RVE with periodic boundary conditions, a and a_c do not differ significantly. Comparing a and a_c between cube and sphere, we find a_c in both cases fall-

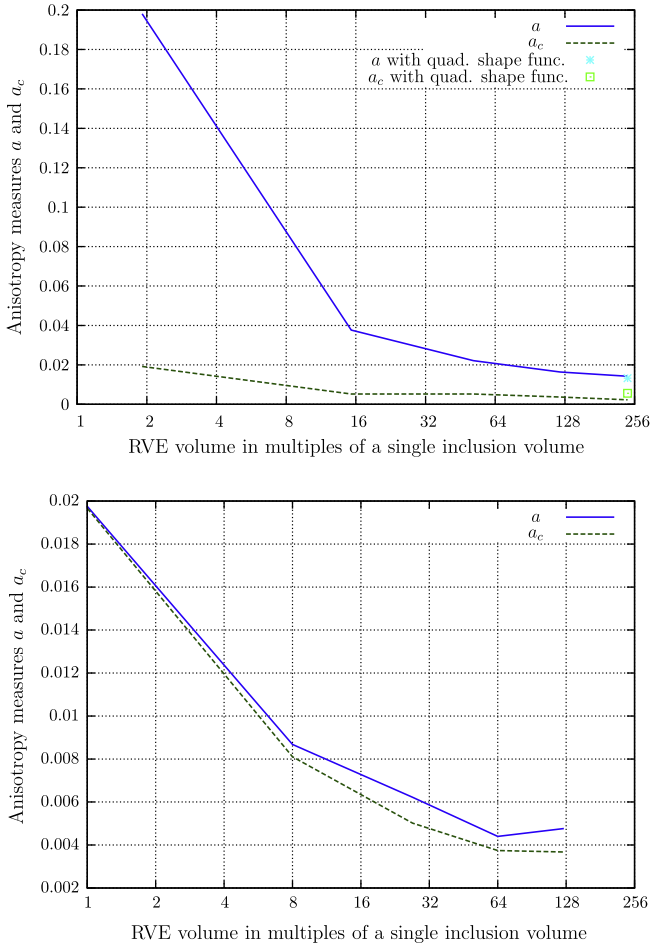

Fig. 5. Anisotropy measures a (filtering out isotropy) and a_c (filtering out cubic anisotropy) for the cubical (upper figure) and the spherical RVE (lower figure).

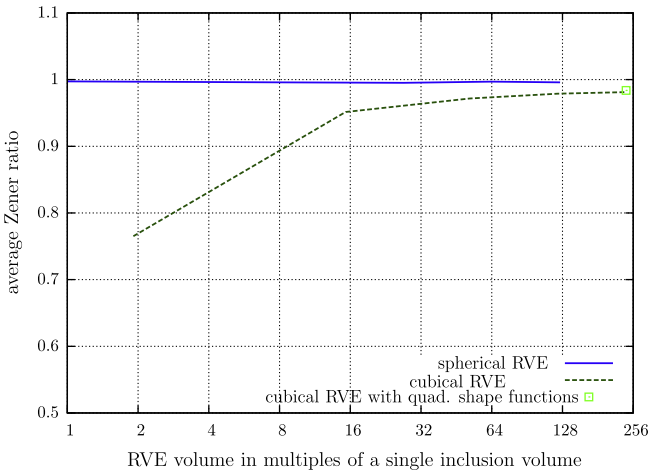

Fig. 6. Zener ratio for spherical and cubical RVE with periodic boundary conditions.

ing from approximately 0.02 for the smallest RVE to approximately 0.005 for the largest RVE. For a, we observe basically the same in case of the sphere, while a starts of at approximately 0.2 for the cubical RVE.

We assessed the influence of the shape functions on the results by repeating the largest RVE calculation with a quadratic hexahedral mesh (Figs. 5 and 6). A slight improvement with respect to the anisotropy has been observed. However, the smallness of the change indicates that the discretization that has been used is sufficient, i.e., the main result is unaffected.

8. Localization behavior

In case of non-quasi-convex incremental stress potentials, structural failure of the RVE may occur. For periodic microstructures, a framework for relating the structural failure of an RVE to a material instability on the macroscale is at hand [32]. For non-periodic microstructures, this issue is still not clear. The reason therefor is twofold:

- While linear displacement boundary conditions prevent localizations to reach the boundary, homogeneous traction boundary conditions allow for an arbitrary deformation of the boundary of the RVE. The periodic boundary conditions, applied to periodically repeatable unit cells, allow for a localization pattern that fits the periodicity frame. Thus, the RVE localization depends on the arbitrary orientation of the periodicity frame. The apparent material should, however, be attained independently on these choices as the size of the RVE is increased.
- As a RVE-wide localization takes place, the representativity of the RVE is lost.

Despite this problems, predictions of macroscopic fracture [1,39], macroscale traction separation laws [35] and forming limit diagrams [21] are obtained by the RVE method, mostly by using cubical RVE with periodic boundary conditions. While most authors demonstrate convergence by considering larger RVE, it is not shown whether the results are sensitive to changes of the RVE shape, the boundary conditions and, in case of periodic boundary conditions, the orientation of the periodicity frame. Just recently, the development of numerical homogenization schemes that overcome the dependence on the orientation of the periodicity frame is approached by Coenen et al. [7], Nguyen et al. [36], who adapt the boundary conditions during the simulation to the specific localization pattern that is encountered. These are termed by Coenen et al. [7] as percolation path boundary conditions.

Since the periodic boundary conditions enjoy some popularity for the prediction of macroscale material failure, this section is dedicated to the study of the localization behavior of spherical and cubical RVE with periodic boundary conditions.

8.1. Simulation setup and material parameters

We start by considering a simple shear deformation with a shear number $\bar{\gamma} = 1$,

$$\overline{\boldsymbol{H}} = \boldsymbol{d} \otimes \boldsymbol{n}, \tag{64}$$

$$\boldsymbol{d} = \cos\alpha \boldsymbol{e}_1 + \sin\alpha \boldsymbol{e}_2, \tag{65}$$

$$\boldsymbol{n} = -\sin\alpha \boldsymbol{e}_1 + \cos\alpha \boldsymbol{e}_2. \tag{66}$$

We applied $\overline{\boldsymbol{H}}$ with $\bar{\gamma}$ growing time-proportional from 0 to 1, with α between 0° and 45°, in steps of 5°, to cubical and spherical RVE with periodic boundary conditions. The material under consideration was the ABAQUS internal, elastic isotropic (E = 5000 MPa, ν = 0.3), von Mises plastic material with σ_{flow} initially at 10 MPa, decaying linearly to 5 MPa at 100% of plastic strain. Beyond 100% of plastic strain, σ_{flow} is constant. The mesh resolution was 20 elements along

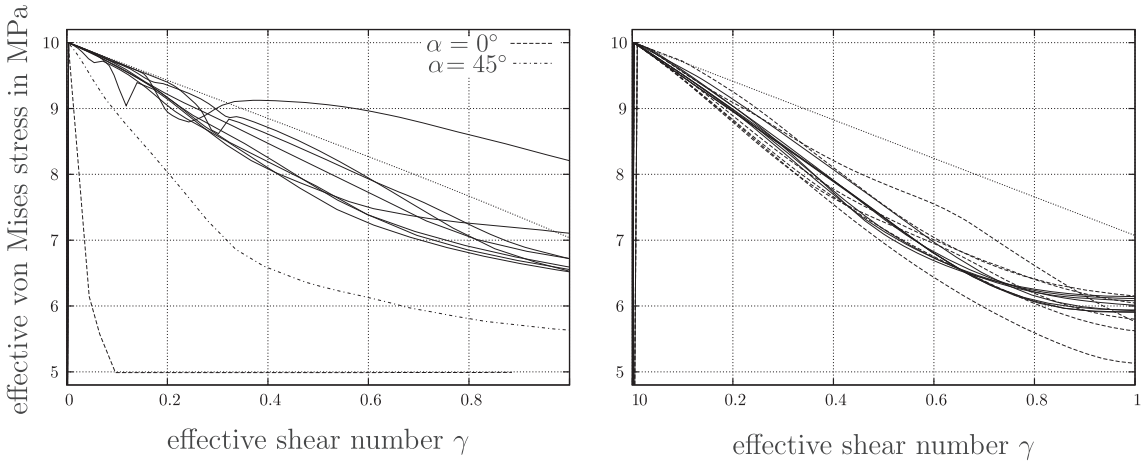

Fig. 7. Von Mises equivalent stress for the shear test in the cubical (left) and spherical (right) RVE with periodic boundary conditions. In the left figure, the dashed lines correspond to the shear directions 0° and 45°. In the right figure, the solid and dashed lines correspond to the cases where the lamination is parallel (eight curves) and perpendicular (six curves) to the effective shear direction, respectively. The dotted lines correspond to the homogeneous deformation of the RVE, enforced by linear displacement boundary conditions.

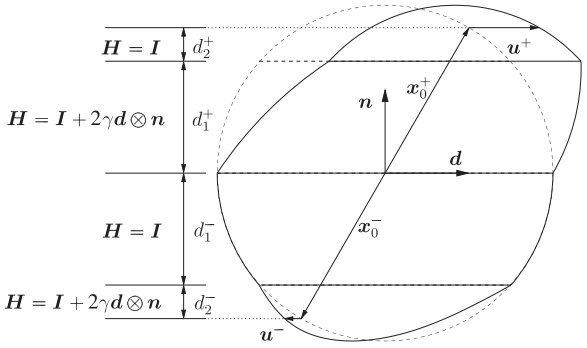

Fig. 8. Schematic figure of a layer decomposition of a spherical RVE, with homogeneously deformed layers.

one edge for the cubical and 20 elements along the diameter for the spherical RVE. We used hexahedral elements with quadratic shape functions (element type C3D20), in order to reduce tendency of a mesh-conform alignment of the shear bands. For a controlled initiation of the localization, in one element the flow stress has been reduced 9 MPa, which has been selected randomly from the list of elements. If the simulations are carried out without perturbing the homogeneous material, the localization is initiated by unavoidable numerical errors.

8.2. Results

The resulting effective equivalent von Mises stress is given in Fig. 7. While the spherical RVEs display only a slight variation, in case of the cubical RVEs a wide variation of the stress–strain curve is observed. The reason therefor is that the localization behavior differs markedly for cubical and spherical RVE.

8.2.1. Behavior of the spherical RVEs

We observed two distinct deformation patterns. These have in common that the sphere is divided into an even number of layers (mostly four layers, at most we observed eight layers). From the resulting odd number of parallel interfaces, one coincides with an equatorial plane, dividing the sphere into two hemispheres. The remaining interfaces are placed symmetrically in the two hemispheres. The layer decomposition takes place either parallel or perpendicular to the effective shear plane $\boldsymbol{n}$. In both cases, the layers alternate between almost undeformed and strongly deformed.

8.2.1.1. Lamination parallel to the effective shear plane. In case of a lamination parallel to the effective shear direction, the deforming layers display an almost homogeneous shearing near the layer interface and the RVE surface, with $\bar{\boldsymbol{H}} = 2\bar{\gamma}\boldsymbol{d} \otimes \boldsymbol{n}$. In the bulk of the layers, a further layer decomposition is observed, see Fig. 9. A sketch with four layers is given in Fig. 8, with the layer thicknesses $d_2^+ = d_2^-$ and $d_1^+ = d_1^-$ and the shear deformation in the first layer on the plus and the second layer on the minus side. One can easily see, by picking two opposing surface points $\boldsymbol{x}_0^\pm$ and calculating the displacements $\boldsymbol{u}^\pm$, that this results in the imposed average deformation and compliance with the periodic boundary conditions,

$$\boldsymbol{u}^+ - \boldsymbol{u}^- = f^+ 2\bar{\gamma}\boldsymbol{d} \otimes \boldsymbol{n} \cdot \boldsymbol{x}_0^+ - f^- 2\bar{\gamma}\boldsymbol{d} \otimes \boldsymbol{n} \cdot \boldsymbol{x}_0^-. \tag{67}$$

The factors $f^\pm$ give fractions of the projected length $(\boldsymbol{n} \cdot \boldsymbol{x}_0)\boldsymbol{n}$ that passes layers that are subjected to the displacement gradient $2\bar{\gamma}\boldsymbol{d} \otimes \boldsymbol{n}$. Due to the described arrangement of the layers we have $f^- = 1 - f^+$. Summarizing with $\boldsymbol{x}_0^- = -\boldsymbol{x}_0^+$ gives

$$\begin{aligned} \boldsymbol{u}^+ - \boldsymbol{u}^- &= f^+ 2\bar{\gamma}\boldsymbol{d} \otimes \boldsymbol{n} \cdot \boldsymbol{x}_0^+ + (1 - f^+) 2\bar{\gamma}\boldsymbol{d} \otimes \boldsymbol{n} \cdot \boldsymbol{x}_0^+ && (68)\\ &= 2\bar{\gamma}\boldsymbol{d} \otimes \boldsymbol{n} \cdot \boldsymbol{x}_0^+ && (69)\\ &= \bar{\gamma}\boldsymbol{d} \otimes \boldsymbol{n} \cdot \left(\boldsymbol{x}_0^+ - \boldsymbol{x}_0^-\right) = \bar{\boldsymbol{H}}\left(\boldsymbol{x}_0^+ - \boldsymbol{x}_0^-\right). && (70) \end{aligned}$$

8.2.1.2. Lamination perpendicular to the effective shear plane. The overall behavior is quite similar compared to the first case. However, the deformation near the layer interfaces and the RVE surface is less homogeneous. Also, the interfaces undergo a more pronounced bending. Fig. 11 allows for a direct comparison of the two deformation patterns. We did not observe any localization that does not fit into one of these schemes. A variation of the magnitude and the location of the perturbation did not have any notable effect on the effective material behavior. Also, no regularity could be found in which of the two described localization schemes is activated.

8.2.2. Behavior of the cubical RVEs

One can find a large number of cubical RVE with periodic boundary conditions undergoing localization in the literature, e.g., Miehe [30], Böhlke et al. [4], Nguyen et al. [35]. At the onset of localization, we observed the formation of a single shear band of constant thickness, the deformation of which growing time-proportional. However, the shear band has to fit the periodicity frame, and is therefore not necessarily parallel to the imposed effective shear direction. Thus, the effective shear strain is approximated by a shifting between differently oriented shear bands (Fig. 10). The change of the active shear band is accompanied by a stiffening

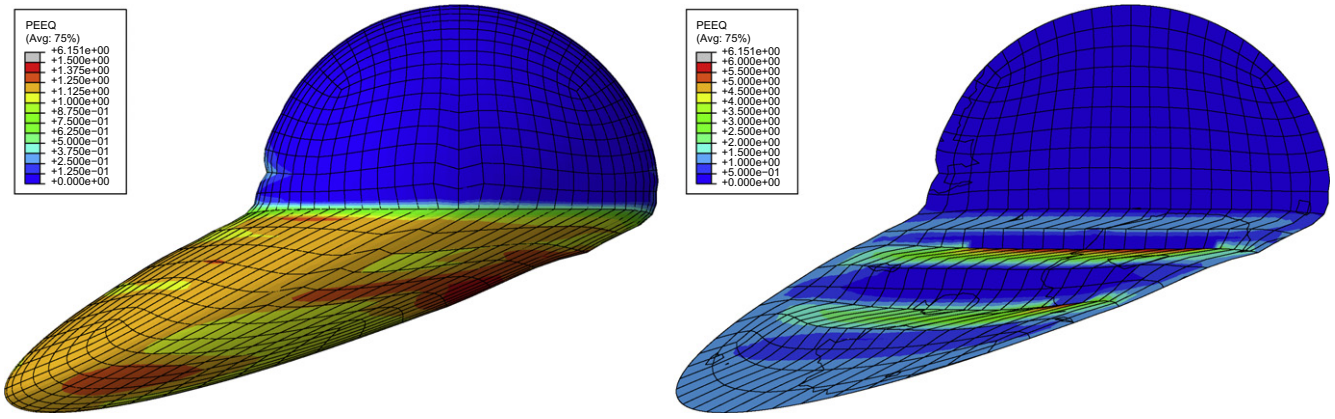

Fig. 9. Localization of the spherical RVE with lamination parallel to the effective shear direction ($\alpha = 0°$) at $\bar{\gamma} = 1$. The color map indicates the equivalent plastic strain between 0 and 1.5 on the left (surface) and 0 and 6 on the right (cut). (For interpretation of the references to color in this figure legend, the reader is referred to the web version of this article.)

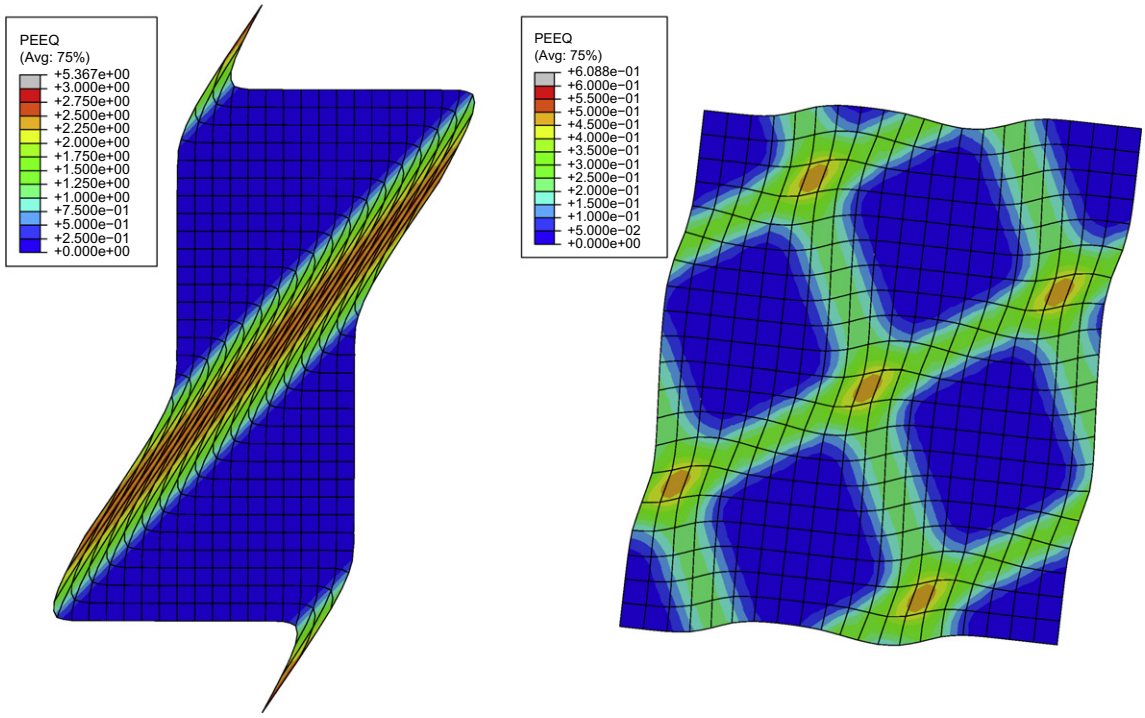

Fig. 10. Localization of the cubical RVE. The color map indicates the equivalent plastic strain. Left: $\bar{\gamma} = 1,\ \alpha = 45^\circ,\ 0 < \varepsilon_{\mathrm{PEEQ}} < 3$. Right: $\bar{\gamma} = 0.216,\ \alpha = 25^\circ,\ 0 < \varepsilon_{\mathrm{PEEQ}} < 0.5$. (For interpretation of the references to color in this figure legend, the reader is referred to the web version of this article.)

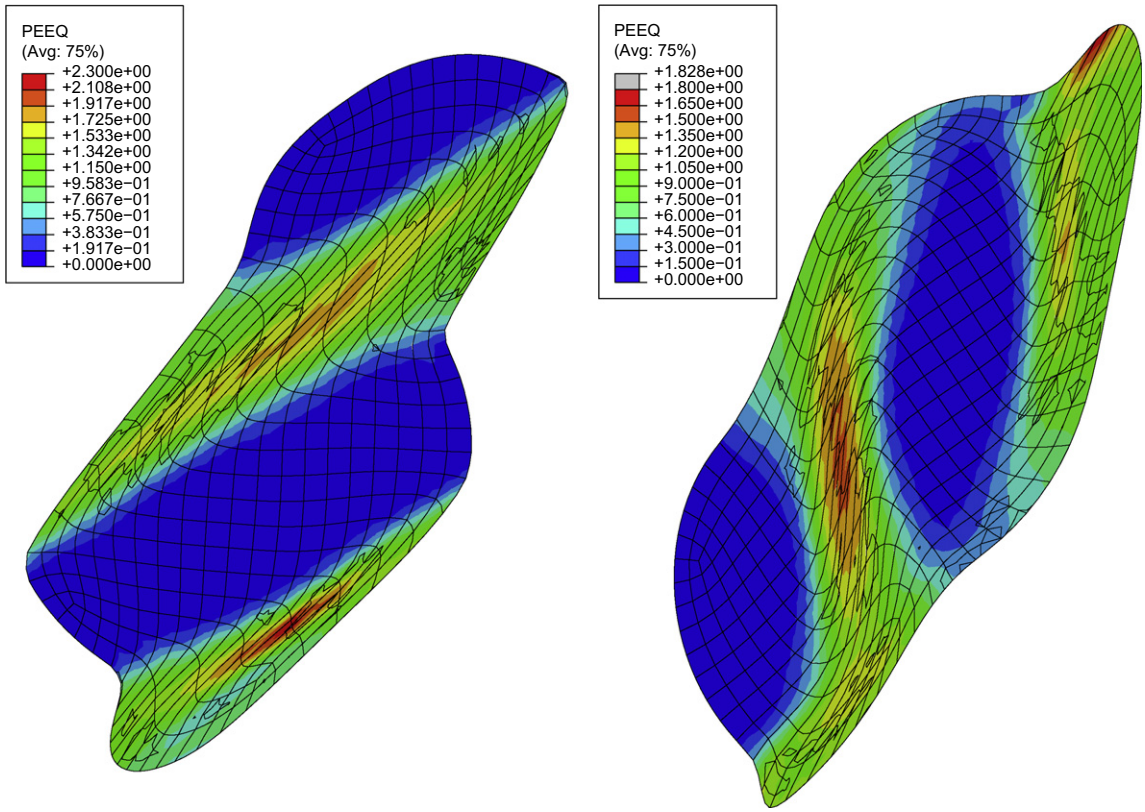

Fig. 11. Cut through localization of the spherical RVE for $\alpha = 30^\circ$ and $\bar{\gamma} = 1$. The color map indicates the equivalent plastic strain, $0 < \varepsilon_{\mathrm{PEEQ}} < 2.3$ on the left and $0 < \varepsilon_{\mathrm{PEEQ}} < 1.8$ on the right. On the left, the lamination is parallel to the effective shear plane, on the right lamination started perpendicular to the effective shear plane, but during the deformation the shear direction changes locally. (For interpretation of the references to color in this figure legend, the reader is referred to the web version of this article.)

effect, which induced the spikes in the stress–strain curves (Fig. 7). The stiffening due to the successive shearing in two different directions exceeds even the response of the homogeneous material. Only in the cases $\alpha = 0°$ and $\alpha = 45°$, a single shear band persisted. Accordingly, the stress–strain curves indicate the softest effective material for this two cases. This is most pronounced for the case $\alpha = 0°$, where the shear band alignment parallel to the mesh interface results in a concentration of the shear band in a single element layer. A variation of the position of the perturbation does not have any effect in case of the cubical RVE, it corresponds to a mere shift of the periodicity frame. Likewise, the magnitude of the perturbation has no notable influence.

8.2.3. Discussion of the localization behavior

It is evident that the orientation of the periodicity frame strongly affects the results in case of the cubical RVE, inducing a scattering of the effective stress strain curve. This is not observed in case of spherical RVE. However, the applicability of the periodic boundary conditions is disputable in both cases. In both cases, even if the perturbation is left out, localization is observed, triggered by numerical round off errors, i.e., stability of the effective material response with respect to small perturbations is not attained. Thus, with the dictum that an RVE should conduct the microscale material behavior "as is" to the macroscale when the material is homogeneous, neither the cubic nor the spherical RVE with periodic boundary conditions give satisfactory results for the softening material. Only the linear displacement boundary conditions satisfy the latter requirement. Then, no difference between cubical and spherical RVE is observed.

9. Summary

We compared the performance of spherical and cubical RVE with different boundary conditions, applied to a macroscopically isotropic matrix–inclusion material with hard elastic inclusions and a soft elastoplastic matrix. It is argued that the periodic boundary conditions are not restricted to periodically repeatable unit cells, although the denomination "periodic" is misleading when applied to non-periodic shapes. Then one should speak more generally of coupled boundary conditions.

We could identify basically two features that distinguish the spherical and the cubical RVE, namely different surface to volume ratio and, in case of periodic boundary conditions, the presence or absence of a periodicity frame. The smaller surface to volume ratio of the spheres result in a smaller influence of the boundary, leading to a better convergence to the effective material behavior. The presence of a periodicity frame in case of the cubical RVE results in a bias of the material anisotropy, which affects the elastic and plastic material properties. To study the convergence and RVE induced anisotropy, we considered macroscopically isotropic matrix-inclusion material.

Considering the rate of convergence to the effective material behavior, for linear displacement boundary conditions, results of similar quality require the cubical RVE to have a volume approximately two to three times that the corresponding spherical RVE. This applies to the elastic and the plastic properties, over the entire range of sizes that has been considered. This behavior is less pronounced for the periodic boundary conditions. It is a result of the smaller surface-to-volume ratio of a sphere compared to a cube of equal volume. For the homogeneous traction boundary conditions, only the elastic properties have been considered, which display almost no difference between spherical and cubical RVE. A comprehensive analysis of the scattering in case of spherical and cubical RVE cannot be delivered, since this requires a much larger amount of data. It is only noted that no clear tendency in favor or against one of the RVE shapes is observed, and that the homogeneous traction boundary conditions appear to result in a reduced scattering of the elastic properties.

Examining the elastic properties of the isotropic macroscale material allows to quantify the spurious cubic anisotropy induced by cubical RVE with periodic boundary conditions. This artificial anisotropy vanishes as the size of the RVE tends to infinity. However, we found that the convergence is quite slow, requiring large RVE. Thus, the cubical shape affects the smallest RVE size which one may consider as sufficiently large to perform sample averaging. If the RVE size is to small, a systematic bias of the anisotropy is induced, which cannot be separated from the effective material properties. This issue can be avoided a priori by using spherical RVE. Other strategies to reduce this effect could be the examination of randomly oriented cubical RVE, where the cubic anisotropy should cancel out in the average, or the application of uniform boundary conditions, which converge slower to the effective material behavior.

Since cubical RVE with periodic boundary conditions that undergo structural failure are commonly used for the prediction of effective material failure and softening, we studied the localization behavior of spherical and cubical RVE with periodic (resp. coupled) boundary conditions. We employed these on a homogeneous, isotropic, softening, elastoplastic material with a small perturbation. It is found that the response of the cubical RVEs depends strongly on the orientation of the periodicity frame. The dependence on the magnitude and position of the perturbation is rather weak. This specific bias is not observed for the spherical RVE, due to the missing periodicity frame. However, the applicability of periodic boundary conditions appears problematic in both cases, since only for linear displacement boundary conditions the material behavior of the quasi homogeneous RVE is conducted "as is" to the macroscale.

In conclusion, the use of spherical RVE is advantageous in case of a random microstructure. For regular microstructures, RVEs that account for the periodicity of the microstructure suit better. In case of localization, the use of spherical instead of cubical RVEs with periodic boundary conditions eliminates the periodicity frame that restricts the localization mode, similarly to the technique proposed by Coenen et al. [7]. However, the use of RVEs that undergo localization for the prediction of effective material failure remains doubtful.

Acknowledgements

We gratefully acknowledge valuable remarks from Jan Kalisch, Felix Fritzen and Thomas Böhlke. Also, we like to express our gratitude to an unknown reviewer for his/her comments.

Appendix A

The requirements (60) and (61) are basically taken care of by mapping $\mathbb{C}$ to $\mathbb{D}$ (Eq. (59)), where only $\mathbb{D}(\mathbb{C}) = -\mathbb{D}(\mathbb{C}^{-1})$ prevents the fulfillment of Eq. (61). However, the minus is taken care of by $a(\mathbb{D}) = a(-\mathbb{D})$ (Eq. (58)).

Specifically, the first mapping to the unimodular part $\mathbb{C}^\circ = \det(\mathbb{C})^{-\frac{1}{6}}\mathbb{C}$ ensures the invariance $a(\mathbb{C}) = a(\alpha\mathbb{C})$. The logarithm $\mathbb{C}^* = \ln \mathbb{C}^\circ$ ensures that inverting $\mathbb{C}$ results merely in a change of sign of the eigenvalues of $\mathbb{C}^*$. Then normalizing $\mathbb{C}^*$ gives $\mathbb{D}$. Due to this normalization, the measure a has the nice property of ranging from 0 (isotropy) to 1 (most anisotropic). This can be seen by noting that

$$\|\mathbb{D} - (\mathbb{P}_1 \cdots \mathbb{D})\mathbb{P}_1 - \frac{1}{5}(\mathbb{P}_2 \cdots \mathbb{D})\mathbb{P}_2\| < 1, \tag{71}$$

since subtracting a projection of a tensor from the tensor itself must result in a tensor with equal or lower norm. One can see that the isotropic part $(\mathbb{P}_1 \cdot\cdot\cdot\cdot \mathbb{D})\mathbb{P}_1 + \frac{1}{5}(\mathbb{P}_2 \cdot\cdot\cdot\cdot \mathbb{D})\mathbb{P}_2$ can indeed be zero: $\mathbb{D} = \sum d_i \mathbb{E}_i$ is traceless due to the logarithm on the unimodular $\mathbb{C}^\circ$, i.e. the eigenvalues d_i sum up to zero. Thus, with the abbreviations

$$\alpha_1 = \mathbb{P}_1 \cdot\cdot\cdot\cdot \mathbb{D} = \sum d_i p_i, \quad p_i = \mathbb{E}_i \cdot\cdot\cdot\cdot \mathbb{P}_1 \tag{72}$$

$$\alpha_2 = \mathbb{P}_2 \cdot\cdot\cdot\cdot \mathbb{D} = \sum d_i (1 - p_i) \tag{73}$$

we have $\alpha_1 + \alpha_2 = \sum d_i = 0$, i.e. if α_1 vanishes the isotropic part of $\mathbb{D}$ is zero. With the restrictions $\mathbb{I} \cdot\cdot\cdot\cdot \mathbb{P}_1 = 1 = \sum p_i$ and all $p_i > 0$ one can find arbitrary many eigenprojectors $\mathbb{E}_i$ such that α_1 vanishes, for example all $p_i = 1/6$.

References

[1] H.Y. Agha, F. Hild, R. Billardon, Microscopic and mesoscopic damage localization, ASTM Special Technical Publication 1315 (1997) 119–130.
[2] A. Bertram, Elasticity and Plasticity of Large Deformations – An Introduction, third ed., Springer Verlag, Berlin, 2012.
[3] T. Böhlke, Crystallographic Texture Evolution and Elastic Anisotropy – Simulation, Modeling and Applications, Shaker Verlag, 2001.
[4] T. Böhlke, G. Bondár, Y. Estrin, M. Lebyodkin, Computational Materials Science 44 (2009) 1076–1088.
[5] T. Böhlke, R. Glüge, B. Klöden, W. Skrotzki, A. Bertram, Modelling and Simulation in Materials Science and Engineering 15 (2007) 619–637.
[6] N. Chawla, Y.-L. Shen, Advanced Engineering Materials 3 (6) (2001) 357–370.
[7] E.W.C. Coenen, V.G. Kouznetsova, M.G.D. Geers, International Journal for Numerical Methods in Engineering 90 (2012) 1–21.
[8] D. Durdban, T. Cohen, Y. Hollander, Mechanics Research Communications 37 (2010) 636–641.
[9] F. Feyel, J.-L. Chaboche, Computer Methods in Applied Mechanics and Engineering 183 (2000) 309–330.
[10] J. Fish, R. Fan, International Journal for Numerical Methods in Engineering 76 (2008) 1044–1064.
[11] F. Fritzen, T. Böhlke, Technische Mechanik 30 (4) (2010) 354–363.
[12] F. Fritzen, T. Böhlke, International Journal for Numerical Methods in Engineering 84 (2010) 803–829.
[13] F. Fritzen, S. Forest, T. Böhlke, D. Kondo, T. Kanit, International Journal of Plasticity 29 (0) (2012) 102–119.
[14] M. Galli, J. Botsis, J. Janczak-Rusch, Computational Materials Science 41 (3) (2008) 312–321.
[15] R. Glüge, Revista chilena de ingeniería 18 (2010) 395–400.
[16] R. Grasset-Bourdel, A. Alzina, N. Tessier-Doyen, N. Schmitt, M. Huger, T. Chotard, Computational Materials Science 50 (2011) 3136–3144.
[17] A. Gurson, Journal of Engineering Materials and Technology 99 (1977) 2–15.
[18] Z. Hashin, Journal of Applied Mechanics 50 (1983) 481–505.
[19] S. Hazanov, C. Huet, Journal of the Mechanics and Physics of Solids 42 (12) (1994) 1995–2011.
[20] R. Hill, Proceedings of the Royal Society of London A 65 (1952) 349–354.
[21] M.F. Horstemeyer, V. Revelli, Stress history dependent localization and failure using continuum damage mechanics concepts, ASTM Special Technical Publication 1315 (1997) 216–237.
[22] H. Inglis, P. Geubelle, K. Matous, Philosophical Magazine 88 (16) (2008) 2373–2397.
[23] T. Kanit, S. Forest, I. Galliet, V. Mounoury, D. Jeulin, International Journal of Solids and Structures 40 (2003) 3647–3679.
[24] Z. Khisaeva, M. Ostoja-Starzewski, Proceedings of the Royal Society of London A 462 (2006) 1167–1180.
[25] S.-J. Kim, J. Choi, M.K. Kwak, Computational Mechanics 31 (2003) 469–478.
[26] B. Klusemann, B. Svendsen, Technische Mechanik 30 (4) (2010) 374–386.
[27] A. Krawietz, Materialtheorie, Springer Verlag, Berlin, 1986.
[28] S. Mesarovic, J. Padbidri, Philosophical Magazine 85 (2005) 65–78.
[29] J. Michel, P. Suquet, International Journal of Solids and Structures 40 (2003) 6937–6955.
[30] C. Miehe, International Journal for Numerical Methods in Engineering 55 (2002) 1285–1322.
[31] C. Miehe, Computer Methods in Applied Mechanics and Engineering 192 (2003) 559–591.
[32] C. Miehe, J. Schröder, M. Becker, Computer Methods in Applied Mechanics and Engineering 191 (2002) 4971–5005.
[33] S. Nemat-Nasser, Mechanics of Materials 31 (1999) 493–523.
[34] V.-D. Nguyen, E. Béchet, C. Geuzaine, L. Noels, Computational Materials Science 55 (0) (2012) 390–406.
[35] V.P. Nguyen, O. Lloberas-Valls, M. Stroeven, L. Sluys, Computer Methods in Applied Mechanics and Engineering 200 (9–12) (2011) 1220–1236.
[36] V.P. Nguyen, M. Stroeven, L.J. Sluys, Engineering Fracture Mechanics 79 (2012) 78–102.
[37] M. Ortiz, E. Repetto, Journal of the Mechanics and Physics of Solids 47 (1999) 397–462.
[38] I. Özdemir, W. Brekelmans, M. Geers, Computer Methods in Applied Mechanics and Engineering 198 (2008) 602–613.
[39] C. Pelissou, J. Baccou, Y. Monrie, F. Perales, International Journal of Solids and Structures 46 (2009) 2842–2855.
[40] K. Rajagopal, Zeitschrift für angewandte Mathematik und Physik ZAMP 58 (2) (2007) 309–317.
[41] A. Salahouelhadj, H. Haddadi, Computational Materials Science 48 (3) (2010) 447–455.
[42] J. Schröder, D. Balzani, D. Brands, Archive of Applied Mechanics 81 (2011) 975–997.
[43] L. Shen, S. Yi , International Journal of Solids and Structures 37 (2000). 3525–3534.
[44] R. Smit, W. Brekelmans, H. Meijer, Computer Methods in Applied Mechanics and Engineering 155 (1998) 181–192.
[45] P. Suquet, Homogenization techniques for composite media, in: Lectures Delivered at the CISM International Center for Mechanical Sciences Udine, Italy, July 1–5, 1985, Lecture Notes in Physics, vol. 272, Springer-Verlag, Berlin, 1987, pp. 199–208 (Ch. Averages, Boundary condition).
[46] B. Svendsen, A. Bertram, Acta Mechanica 132 (0) (1999) 195–207.
[47] X. Xu, X. Chen, Mechanics of Materials 41 (2009) 174–186.
[48] C. Zener, Physical Review 71 (12) (1947) 846–851.
[49] T. Zohdi, P. Wriggers, Introduction to Computational Micromechanics, Lecture Notes in Applied and Computational Mechanics, Springer, 2005.